

Pion form factors from two-flavor lattice QCD with exact chiral symmetry

S. Aoki^{a,b}, T. W. Chiu^c, H. Fukaya^d, S. Hashimoto^{e,f}, T. H. Hsieh^g, T. Kaneko^{e,f},
H. Matsufuru^h, J. Noaki^e, T. Onogiⁱ, E. Shintaniⁱ and N. Yamada^{e,f}

(JLQCD and TWQCD collaborations)

^a*Graduate School of Pure and Applied Sciences,
University of Tsukuba, Ibaraki 305-8571, Japan*

^b*Riken BNL Research Center, Brookhaven National Laboratory, Upton, New York 11973, USA*

^c*Physics Department, Center for Theoretical Sciences,
and Center for Quantum Science and Engineering,
National Taiwan University, Taipei, 10617, Taiwan*

^d*Department of Physics, Nagoya University, Nagoya 464-8602, Japan*

^e*KEK Theory Center, High Energy Accelerator Research Organization (KEK), Ibaraki 305-0801, Japan*

^f*School of High Energy Accelerator Science,*

The Graduate University for Advanced Studies (Sokendai), Ibaraki 305-0801, Japan

^g*Research Center for Applied Sciences, Academia Sinica, Taipei 115, Taiwan*

^h*Computing Research Center, High Energy Accelerator
Research Organization (KEK), Ibaraki 305-0801, Japan*

ⁱ*Yukawa Institute for Theoretical Physics,
Kyoto University, Kyoto 606-8502, Japan*

(Dated: February 19, 2013)

We calculate pion vector and scalar form factors in two-flavor lattice QCD and study the chiral behavior of the vector and scalar radii $\langle r^2 \rangle_{V,S}$. Numerical simulations are carried out on a $16^3 \times 32$ lattice at a lattice spacing of 0.12 fm with quark masses down to $\sim m_s/6$, where m_s is the physical strange quark mass. Chiral symmetry, which is essential for a direct comparison with chiral perturbation theory (ChPT), is exactly preserved in our calculation at finite lattice spacing by employing the overlap quark action. We utilize the so-called all-to-all quark propagator in order to calculate the scalar form factor including the contributions of disconnected diagrams and to improve statistical accuracy of the form factors. A detailed comparison with ChPT reveals that the next-to-next-to-leading-order contributions to the radii are essential to describe their chiral behavior in the region of quark mass from $m_s/6$ to $m_s/2$. Chiral extrapolation based on two-loop ChPT yields $\langle r^2 \rangle_V = 0.409(23)(37) \text{ fm}^2$ and $\langle r^2 \rangle_S = 0.617(79)(66) \text{ fm}^2$, which are consistent with phenomenological analysis. We also present our estimates of relevant low-energy constants.

I. INTRODUCTION

Recent algorithmic improvements allow us to perform large-scale simulations of unquenched QCD in the chiral regime with various lattice discretizations. Calculation of phenomenologically important quantities has then become feasible. In order to make reliable prediction for physical observables, it is crucial to examine the consistency of their chiral behavior with expectations from chiral perturbation theory (ChPT). Lattice QCD with exact chiral symmetry is the cleanest framework for this purpose, while conventional lattice actions may distort chiral behavior of observables by their explicit symmetry breaking, especially when one goes beyond the next-to-leading order (NLO) in ChPT. The JLQCD and TWQCD collaborations embarked on the simulations with exact chiral symmetry [1, 2] employing the overlap quark action [3, 4]. So far, we have performed a detailed study of the pion mass and decay constant in two-flavor lattice QCD [5]. For other physics results from this project, see [6, 7, 8, 9, 10, 11, 12, 13].

The pion vector form factor $F_V(q^2)$ defined by

$$\langle \pi(p') | V_\mu | \pi(p) \rangle = (p + p')_\mu F_V(q^2), \quad q^2 = (p - p')^2, \quad (1)$$

provides a simple testing ground for the consistency between lattice calculation and ChPT. This is one of the fundamental quantities to characterize the low-energy dynamics of pions: for instance, it is related to the charge radius of pion

$$\langle r^2 \rangle_V = 6 \left. \frac{\partial F_V(q^2)}{\partial q^2} \right|_{q^2=0}. \quad (2)$$

The chiral expansion of $F_V(q^2)$ and $\langle r^2 \rangle_V$ is available up to two loops, namely to the next-to-next-to-leading-order (NNLO), both for $N_f = 2$ [14, 15, 16] and $N_f = 3$ [17, 18]. Analyses of experimental data based on two-loop ChPT have led to precise estimates of $\langle r^2 \rangle_V$ [16, 18], which can also be used as a benchmark of lattice calculations.

From previous lattice studies [19, 20, 21, 22, 23, 24, 25, 26, 27], the consistency with experiment has not been established convincingly: some of them reported good agreement with experiment [24, 26, 27], whereas others underestimated $\langle r^2 \rangle_V$ significantly [20, 22, 23, 25]. This is possibly due to systematics in the parametrization of the q^2 dependence of $F_V(q^2)$ and to the chiral extrapolation of $\langle r^2 \rangle_V$. For instance, the NNLO chiral corrections are fully taken into account in the ChPT analyses but not in most of the previous lattice studies. They could significantly modify the chiral behavior of $\langle r^2 \rangle_V$ at up and down quark masses larger than their physical value, as demonstrated in our report [28] and more recently in Ref. [27] with a different

lattice discretization. Our simulations with exact chiral symmetry enable us to perform more stringent test of the chiral behavior of lattice data using two-loop ChPT without suffering from the distortion due to explicit chiral symmetry breaking present in other frameworks.

The chiral behavior of the scalar form factor $F_S(q^2)$ defined by

$$\langle \pi(p') | S | \pi(p) \rangle = F_S(q^2) \quad (3)$$

is another interesting subject, since i) its radius

$$\langle r^2 \rangle_S = 6 \left. \frac{\partial F_S(q^2)}{\partial q^2} \right|_{q^2=0} \quad (4)$$

provides a determination of the low energy constant (LEC) l_4 alternative to that with the decay constant F_π , and ii) $\langle r^2 \rangle_S$ has 6 times enhanced chiral logarithm compared to $\langle r^2 \rangle_V$ and thus may offer an opportunity to clearly identify the one-loop chiral logarithm. Since there are no experimental processes directly related to $F_S(q^2)$, its direct determination is possible only through lattice QCD. It is however difficult to evaluate disconnected correlation functions with conventional point-to-all quark propagator, which flows from a fixed lattice site to any site. There have been only a few calculations of $F_S(q^2)$ [23, 25], and the contributions of disconnected diagrams were ignored in these studies.

In this paper, we calculate the pion vector and scalar form factors $F_{V,S}(q^2)$ in two-flavor QCD and study the chiral behavior of the radii $\langle r^2 \rangle_{V,S}$. For a detailed comparison with two-loop ChPT, we preserve chiral symmetry by employing the overlap quark action and simulate up and down quarks with masses as low as $m \sim m_s/6$. The scalar form factor $F_S(q^2)$ is evaluated including the contribution of disconnected diagrams by using the all-to-all quark propagator, which contains propagations from *any* lattice site to any site. The all-to-all propagator is also helpful to substantially improve statistical accuracy of $F_{V,S}(q^2)$. Our preliminary analyses based on one- and two-loop ChPT have been reported in Refs. [29] and [28], respectively.

This paper is organized as follows. We introduce our simulation method in Sec. II. Calculation of the form factors from pion correlators is presented in Sec. III. We parametrize their q^2 dependence in Sec. IV. Section V is devoted to a detailed description of our chiral extrapolation of the radii. Finally, our concluding remarks are given in Sec. VI.

II. SIMULATION METHOD

A. Configuration generation

We calculate pion form factors in QCD with dynamical up and down quarks with a degenerate mass parameter. Numerical simulations are carried out with the Iwasaki gauge action [30] and the overlap quark action [3, 4], which has exact chiral symmetry at finite lattice spacings [31]. Its Dirac operator is given by

$$D(m) = \left(m_0 + \frac{m}{2}\right) + \left(m_0 - \frac{m}{2}\right) \gamma_5 \text{sgn}[H_W(-m_0)], \quad (5)$$

where m is the quark mass and $H_W(-m_0) = \gamma_5 D_W(-m_0)$ is the Hermitian Wilson-Dirac operator. We set the mass parameter of this kernel operator to $-m_0 = -1.6$, with which the locality of the overlap Dirac operator is confirmed [32, 33]. Because of the sign function $\text{sgn}[H_W(-m_0)]$ in $D(m)$, the overlap action is discontinuous when $H_W(-m_0)$ develops zero eigenvalue(s). The commonly-used Hybrid Monte Carlo (HMC) algorithm can be modified to deal with this discontinuity [34] but turned out to be very costly. In order to carry out high-statistics simulations, we suppress (near-)zero modes of $H_W(-m_0)$ by introducing an auxiliary determinant

$$\Delta_W = \frac{\det[H_W(-m_0)^2]}{\det[H_W(-m_0)^2 + \mu^2]} \quad (6)$$

into the Boltzmann weight [35, 36]. We note that this can be considered as an $O(a^2)$ modification of the gauge action, and hence does not change the continuum limit of the theory. The parameter μ is tuned to 0.2 so as to minimize lattice artifacts induced by Δ_W [32, 36]. We refer readers to Ref. [33] for further details of our simulation method.

An important property of the determinant Δ_W is that it fixes the global topological charge Q of the gauge field during continuous updating of the gauge configuration in the HMC algorithm. Note, however, that local topological fluctuations are present, and the topological susceptibility calculated in Ref. [8] shows expected behavior as a function of sea quark mass. As shown in Refs. [37, 38], the effect of fixed *global* topology can be considered as a finite volume effect and is suppressed by the inverse of the space-time volume V . Furthermore the effect can be systematically corrected by investigating Q dependence of physical observables of interest [38].

Our gauge ensembles are generated on a $16^3 \times 32$ lattice. The bare gauge coupling is $\beta = 6/g^2 = 2.30$ where the lattice spacing determined from the Sommer scale $r_0 = 0.49$ fm [39] is $a = 0.1184(21)$ fm. In the trivial topological sector $Q = 0$, we take four values of bare up and

down quark masses, $m = 0.015, 0.025, 0.035$ and 0.050 , which cover a range $[m_s/6, m_s/2]$. At each m , we calculate pion form factors using 100 independent configurations separated by 100 HMC trajectories. In order to study the effect of fixed topology, we also simulate non-trivial topological sectors $Q = -2$ and -4 at $m = 0.050$ with statistics of 50 independent configurations.

B. Construction of all-to-all quark propagator

The conventional method to calculate hadron correlators employs the so-called point-to-all quark propagator which flows from a fixed lattice site to any site. This is however not suitable to calculate disconnected diagrams which involve quark loops starting from and ending at arbitrary lattice sites. In this work, therefore, we construct all-to-all quark propagator that contains the quark propagating from any lattice site to any site along the strategy proposed in Ref. [40].

Let us consider a decomposition of the quark propagator using eigenmodes of the overlap operator

$$D^{-1}(x, y) = \sum_k \frac{1}{\lambda^{(k)}} u^{(k)}(x) u^{(k)\dagger}(y), \quad (7)$$

where $\lambda^{(k)}$ and $u^{(k)}(x)$ represent k -th lowest eigenvalue and eigenvector of D , respectively. Note that the eigenvalues are ordered by their absolute values. Color and spinor indices are suppressed for simplicity. It is expected that low-lying modes dominate low-energy dynamics of pions including their form factors. We evaluate these low-mode contributions to the propagator *exactly* as

$$(D^{-1})_{\text{low}}(x, y) = \sum_{k=1}^{N_e} \frac{1}{\lambda^{(k)}} u^{(k)}(x) u^{(k)\dagger}(y) \quad (N_e = 100) \quad (8)$$

using 100 low-lying modes for each gauge configuration. Note that the overlap operator is normal and we do not have to distinguish left and right eigenvectors.

The contribution of higher modes is estimated stochastically by the noise method with the dilution technique [40]. We prepare a single Z_2 noise vector $\eta^{(d)}(x)$ for each configuration, and *dilute* it into $N_d = 3 \times 4 \times N_t/2$ vectors, which have non-zero elements only for a single combination of color and spinor indices and at two consecutive time-slices. The high-mode contribution can be estimated as

$$(D^{-1})_{\text{high}}(x, y) = \sum_{d=1}^{N_d} x^{(d)}(x) \eta^{(d)\dagger}(y) \quad (9)$$

by solving a linear equation for each diluted source

$$\sum_y D(x, y) x^{(d)}(y) = \sum_y (\delta_{xy} - P_{\text{low}}(x, y)) \eta^{(d)}(y) \quad (d = 1, \dots, N_d), \quad (10)$$

where d is an index to represent the dilution and

$$P_{\text{low}}(x, y) = \sum_{k=1}^{N_e} u^{(k)}(x) u^{(k)\dagger}(y) \quad (11)$$

is the projector to the eigenspace spanned by the low-modes.

By combining Eqs. (8) and (9), the all-to-all quark propagator can be expressed by a matrix

$$D^{-1}(x, y) = \sum_{k=1}^{N_v} v^{(k)}(x) w^{(k)\dagger}(y) \quad (12)$$

constructed from the following two sets of vectors v and w

$$\left\{ v^{(1)}, \dots, v^{(N_v)} \right\} = \left\{ \frac{u^{(1)}}{\lambda^{(1)}}, \dots, \frac{u^{(N_e)}}{\lambda^{(N_e)}}, x^{(1)}, \dots, x^{(N_d)} \right\}, \quad (13)$$

$$\left\{ w^{(1)}, \dots, w^{(N_v)} \right\} = \left\{ u^{(1)}, \dots, u^{(N_e)}, \eta^{(1)}, \dots, \eta^{(N_d)} \right\}, \quad (14)$$

where $N_v = N_e + N_d$.

C. Measurement of pion correlators

Using the all-to-all propagator (12), the pion two-point function with a temporal separation Δt and a spatial momentum \mathbf{p} can be expressed as

$$C_{\pi\pi, \phi\phi'}(\Delta t; \mathbf{p}) = \frac{1}{N_t} \sum_{t=1}^{N_t} \sum_{k,l=1}^{N_v} \mathcal{O}_{\gamma_5, \phi'}^{(k,l)}(t + \Delta t, \mathbf{p}) \mathcal{O}_{\gamma_5, \phi}^{(l,k)}(t, -\mathbf{p}). \quad (15)$$

Here $\mathcal{O}_{\Gamma, \phi}(t, \mathbf{p})$ is constructed from the v and w vectors as

$$\mathcal{O}_{\Gamma, \phi}^{(k,l)}(t; \mathbf{p}) = \sum_{\mathbf{x}, \mathbf{r}} \phi(\mathbf{r}) w^{(k)\dagger}(\mathbf{x} + \mathbf{r}, t) \Gamma v^{(l)}(\mathbf{x}, t) e^{-i\mathbf{p}\mathbf{x}}, \quad (16)$$

and represents the meson field with a Dirac matrix Γ and a momentum \mathbf{p} at a temporal coordinate t . We use a local $\phi_l(\mathbf{r}) = \delta_{\mathbf{r}, \mathbf{0}}$ and an exponential form $\phi_s(\mathbf{r}) = \exp[-0.4|\mathbf{r}|]$ for the smearing function $\phi(\mathbf{r})$ in this study. Note that the source point \mathbf{x} is averaged over spatial volume.

Pion form factors are extracted from three-point functions shown in Fig. 1, which can also be calculated from the meson fields $\mathcal{O}_{\Gamma, \phi}(t, \mathbf{p})$ as

$$C_{\pi\Gamma\pi}^{(\text{conn})}(\Delta t, \Delta t'; \mathbf{p}, \mathbf{p}') = \frac{1}{N_t} \sum_{t=1}^{N_t} \sum_{k,l,m=1}^{N_v} \mathcal{O}_{\gamma_5, \phi_s}^{(m,l)}(t + \Delta t + \Delta t'; \mathbf{p}') \mathcal{O}_{\Gamma, \phi_l}^{(l,k)}(t + \Delta t; \mathbf{p} - \mathbf{p}') \times \mathcal{O}_{\gamma_5, \phi_s}^{(k,m)}(t; -\mathbf{p}), \quad (17)$$

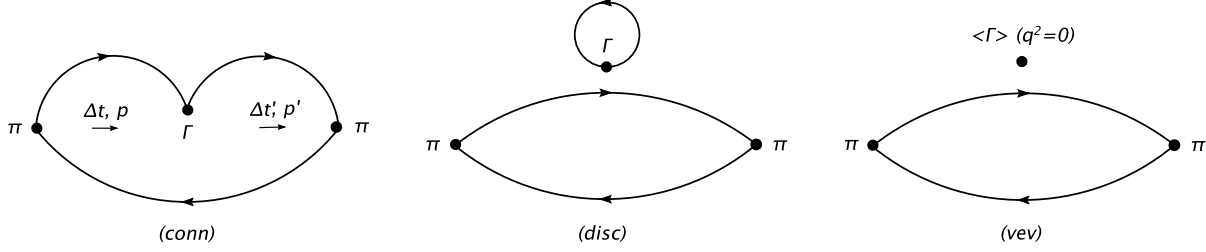


FIG. 1: Connected (left-most diagram) and disconnected three point functions (middle diagram). Note that $F_S(0)$ receives a contribution from the right-most diagram due to the non-zero vacuum expectation value (VEV) of the scalar operator S .

$$C_{\pi\Gamma\pi}^{(\text{disc})}(\Delta t, \Delta t'; \mathbf{p}, \mathbf{p}') = \frac{1}{N_t} \sum_{t=1}^{N_t} \sum_{k,l=1}^{N_v} \mathcal{O}_{\gamma_5, \phi_s}^{(k,l)}(t + \Delta t + \Delta t'; \mathbf{p}') \mathcal{O}_{\gamma_5, \phi_s}^{(l,k)}(t; -\mathbf{p}) \times \sum_{k=1}^{N_v} \mathcal{O}_{\Gamma, \phi_l}^{(k,k)}(t + \Delta t; \mathbf{p} - \mathbf{p}'), \quad (18)$$

$$C_{\pi\Gamma\pi}^{(\text{vev})}(\Delta t, \Delta t'; \mathbf{p}, \mathbf{p}') = \frac{1}{N_t} \sum_{t=1}^{N_t} \sum_{k,l=1}^{N_v} \mathcal{O}_{\gamma_5, \phi_s}^{(k,l)}(t + \Delta t + \Delta t'; \mathbf{p}') \mathcal{O}_{\gamma_5, \phi_s}^{(l,k)}(t; -\mathbf{p}) \times \left\langle \frac{1}{N_t} \sum_{t'=1}^{N_t} \sum_{k=1}^{N_v} \mathcal{O}_{\Gamma, \phi_l}^{(k,k)}(t'; \mathbf{p} - \mathbf{p}') \right\rangle_{\text{conf}}, \quad (19)$$

where $\langle \cdots \rangle_{\text{conf}}$ represents the ensemble average. We denote the temporal separation and spatial momentum for the initial (final) meson by Δt and \mathbf{p} ($\Delta t'$ and \mathbf{p}'), respectively.

We prepare the v and w vectors on the IBM Blue Gene/L at KEK, which has the peak speed of 57.3 TFLOPS. We employ the implicitly restarted Lanczos algorithm to calculate low-modes of D . The computational cost of this step is roughly 0.6 TFLOPS·hours per configuration. Solving Eq. (10) is the most time-consuming part in our measurement, since it requires $N_t/2$ times more inversions than the conventional measurement of two-point functions with the point-to-all propagator. We use the conjugate gradient (CG) algorithm accelerated by the relaxed stopping condition [41] and by the preconditioning using the 100 low-modes. The resulting CPU cost of our CG solver is ~ 1.7 TFLOPS · hours/conf. The calculation of the meson field $\mathcal{O}_{\Gamma, \phi}^{(k,l)}(t, \mathbf{p})$ needs much less CPU time than the above two steps: it is about 0.2 GFLOPS · hours/conf for a single choice of $(m, \mathbf{p}, \Gamma, \phi)$. Once $\mathcal{O}_{\Gamma, \phi}^{(k,l)}(t, \mathbf{p})$ is prepared, we can calculate all of the connected and disconnected pion correlators with small additional cost. These calculations are carried out on the Hitachi SR11000 with the peak speed of 2.15 TFLOPS and workstations at KEK.

It is advantageous that we do not have to repeat the time consuming preparation of v and w vectors to calculate meson fields $\mathcal{O}_{\Gamma, \phi}(t, \mathbf{p})$ with different choices of \mathbf{p} , Γ and ϕ . In order to

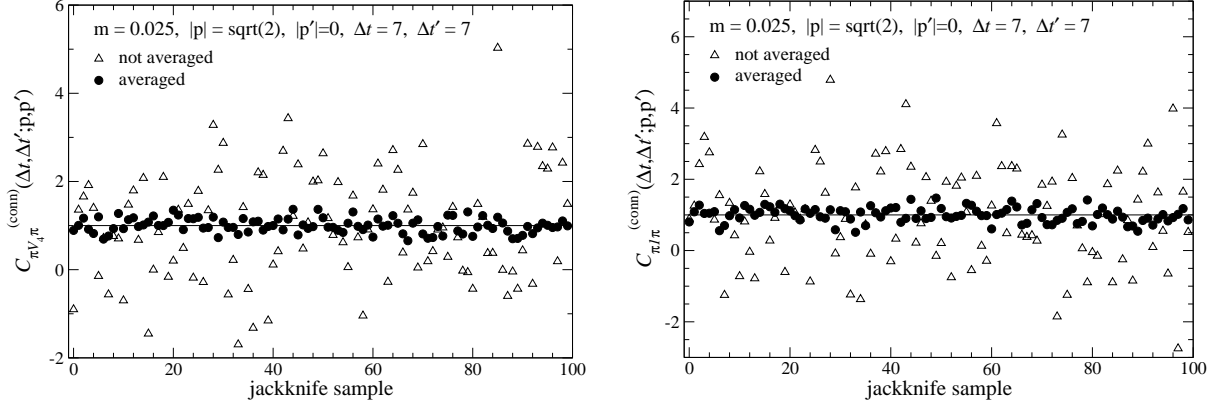


FIG. 2: Statistical fluctuation of connected three point functions $C_{\pi V_4 \pi, \phi_s \phi_s}^{(\text{conn})}(\Delta t, \Delta t'; \mathbf{p}, \mathbf{p}')$ (left panel) and $C_{\pi 1 \pi, \phi_s \phi_s}^{(\text{conn})}(\Delta t, \Delta t'; \mathbf{p}, \mathbf{p}')$ (right panel) with $\Delta t = \Delta t' = 7$, $|\mathbf{p}| = \sqrt{2}$ and $|\mathbf{p}'| = 0$. Open triangles are jackknife data with a single choice of the source location (\mathbf{x}, t) and momentum configuration $(\mathbf{p}, \mathbf{p}')$, whereas the filled squares are averaged over (\mathbf{x}, t) and $(\mathbf{p}, \mathbf{p}')$ corresponding to the same value of q^2 . Each data is normalized by its statistical average.

simulate various values of q^2 , we take 27 choices of the spatial momentum \mathbf{p} with $|\mathbf{p}| \leq \sqrt{3}$ for the initial and final pions, and 33 choices with $|\mathbf{q}| \leq 2$ for the momentum transfer q . Note that the spatial momentum is shown in units of $2\pi/L$ in this article. This setup covers the region of momentum transfer $-1.7 \lesssim q^2 [\text{GeV}^2] \leq 0$.

The use of the all-to-all propagator also improves the statistical accuracy of the pion correlators by averaging over the locations of source operator*, namely (\mathbf{x}, t) in Eqs. (16)–(19), as well as over momentum configurations $(\mathbf{p}, \mathbf{p}')$ corresponding to the same value of q^2 . Figure 2 compares the statistical fluctuation of connected pion correlators with a certain choice of Δt , $\Delta t'$ and q^2 . We observe that averaging over the source locations and momentum configurations remarkably reduces the statistical error of the correlators and leads to very accurate results for the form factors.

* We note in passing that only the low-mode contribution is averaged over the locations of the source operator in the so-called low-mode averaging (LMA) method [42, 43]. The high-mode contribution in LMA is estimated for a fixed source location using the point-to-all propagator in contrast to our method with the all-to-all propagator.

III. DETERMINATION OF PION FORM FACTORS

A. Ratio method for vector form factor

In the limit of large temporal separations among pion operators and vector current, two- and three-point functions are dominated by the contribution from the ground state

$$C_{\pi\pi,\phi\phi'}(\Delta t; \mathbf{p}) \xrightarrow{\Delta t \rightarrow \infty} \frac{Z_{\pi,\phi'}(|\mathbf{p}|)^* Z_{\pi,\phi}(|\mathbf{p}|)}{2 E_\pi(|\mathbf{p}|)} e^{-E_\pi(|\mathbf{p}|) \Delta t}, \quad (20)$$

$$C_{\pi\Gamma\pi}^{(\text{conn})}(\Delta t, \Delta t'; \mathbf{p}, \mathbf{p}') \xrightarrow{\Delta t, \Delta t' \rightarrow \infty} \frac{Z_{\pi,\phi'}(|\mathbf{p}'|)^* Z_{\pi,\phi}(|\mathbf{p}|)}{4 E_\pi(|\mathbf{p}'|) E_\pi(|\mathbf{p}|)} \frac{1}{Z_V} \langle \pi(p') | V_\mu | \pi(p) \rangle \times e^{-E_\pi(|\mathbf{p}'|) \Delta t'} e^{-E_\pi(|\mathbf{p}|) \Delta t}, \quad (21)$$

where $Z_{\pi,\phi}(|\mathbf{p}|) = \langle \pi(p) | \mathcal{O}_{\gamma_5, \phi} \rangle$ is the overlap of the interpolating field $\mathcal{O}_{\gamma_5, \phi}$ to the physical state, and Z_V is the renormalization factor for the vector current. For a precise determination of the matrix element $\langle \pi(p') | V_\mu | \pi(p) \rangle$, it is advantageous to take a ratio of appropriately chosen correlators in order to cancel out the exponential damping factors $e^{-E_\pi(|\mathbf{p}'|) \Delta t'}$ and other unnecessary factors $Z_{\pi,\phi^{(\prime)}}$ and Z_V [44]. In this study, we use the following ratio to calculate an effective value of the vector form factor $F_V(q^2)$

$$F_V(\Delta t, \Delta t'; q^2) = \frac{2 M_\pi}{E_\pi(|\mathbf{p}|) + E_\pi(|\mathbf{p}'|)} \frac{R_V(\Delta t, \Delta t'; |\mathbf{p}|, |\mathbf{p}'|, q^2)}{R_V(\Delta t, \Delta t'; 0, 0, 0)}, \quad (22)$$

$$R_V(\Delta t, \Delta t'; |\mathbf{p}|, |\mathbf{p}'|, q^2) = \frac{1}{N_{|\mathbf{p}|, |\mathbf{p}'|}} \sum_{\text{fixed } |\mathbf{p}|, |\mathbf{p}'|} \frac{C_{\pi\gamma_4\pi}^{(\text{conn})}(\Delta t, \Delta t'; \mathbf{p}, \mathbf{p}')}{C_{\pi\pi, \phi_s \phi_l}(\Delta t; \mathbf{p}) C_{\pi\pi, \phi_l \phi_s}(\Delta t'; \mathbf{p}')}, \quad (23)$$

where $(1/N_{|\mathbf{p}|, |\mathbf{p}'|}) \sum_{\text{fixed } |\mathbf{p}|, |\mathbf{p}'|}$ represents the average over momentum configurations corresponding to the same value of q^2 .

The kinematical factor in Eq. (22) involves energies of the initial and final pion states. Effective values of $E_\pi(|\mathbf{p}|)$ at our largest and smallest quark mass are plotted in Figs. 3 and 4. Our data show clear signals up to the largest spatial momentum $|\mathbf{p}| \leq \sqrt{3}$, since their statistical errors are greatly reduced by the use of the all-to-all propagators. We determine $E_\pi(|\mathbf{p}|)$ by a single-cosh fit to $C_{\pi\pi, \phi_s \phi_s}(\Delta t; \mathbf{p})$ with a fit range $\Delta t \in [\Delta t_{\min}, N_t/2]$. The minimum temporal separation Δt_{\min} is chosen by inspecting Δt_{\min} dependence of the fit result. Numerical results for $E_\pi(|\mathbf{p}|)$ are summarized in Table I. They are consistent with the dispersion relation $E_\pi(|\mathbf{p}|) = \sqrt{M_\pi^2 + \mathbf{p}^2}$, which is commonly assumed in previous studies to estimate $E_\pi(|\mathbf{p}|)$ for $|\mathbf{p}| > 0$. In this work, however, we use the measured value of $E_\pi(|\mathbf{p}|)$ in order not to underestimate uncertainty in $E_\pi(|\mathbf{p}|)$ and hence $F_V(\Delta t, \Delta t'; q^2)$.

We extract the vector form factor $F_V(q^2)$ by a constant fit to the effective value

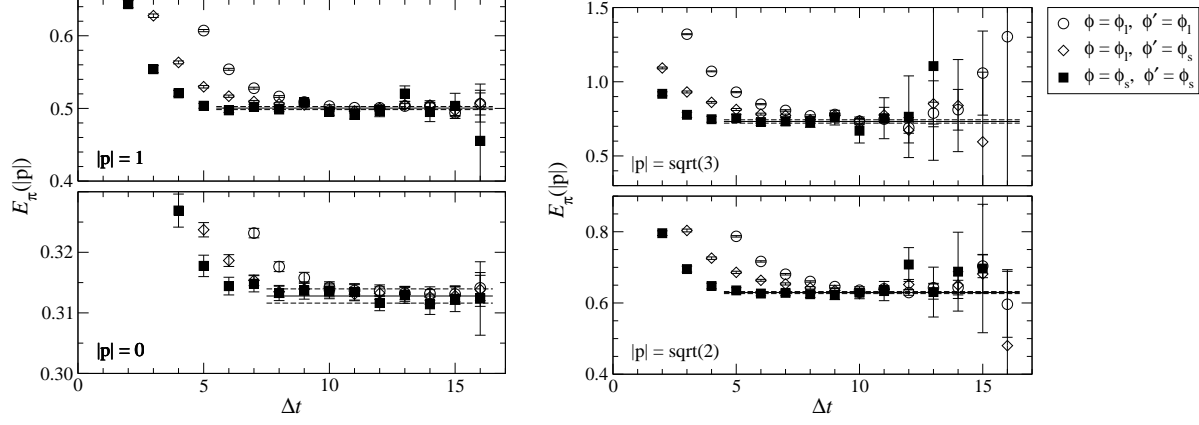


FIG. 3: Effective value of pion energy $E_\pi(|\mathbf{p}|)$ at $(Q, m) = (0, 0.050)$. Circles, triangles and squares show results from $C_{\pi\pi, \phi_l \phi_l}(\Delta t; \mathbf{p})$, $C_{\pi\pi, \phi_l \phi_s}(\Delta t; \mathbf{p})$ and $C_{\pi\pi, \phi_s \phi_s}(\Delta t; \mathbf{p})$, respectively.

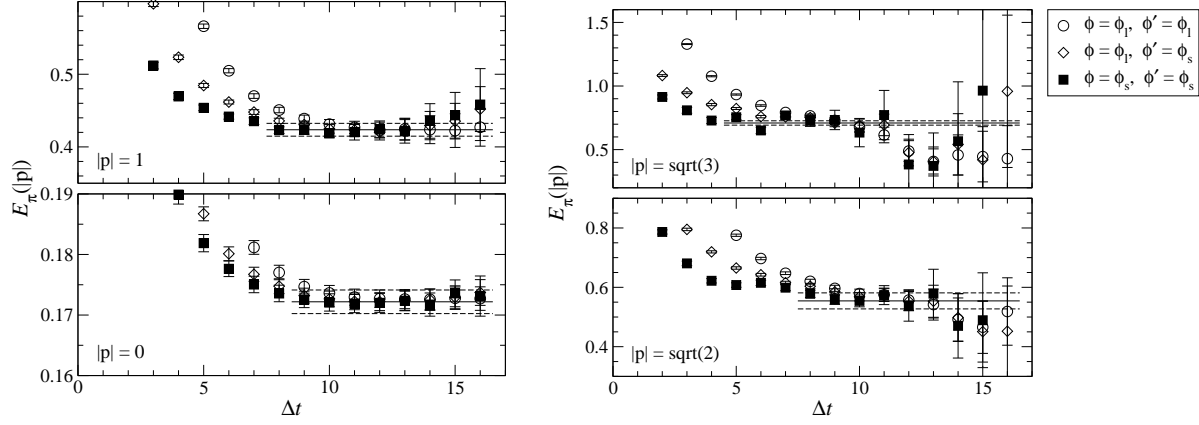


FIG. 4: Effective value of pion energy $E_\pi(|\mathbf{p}|)$ at $(Q, m) = (0, 0.015)$.

TABLE I: Fit results for pion energy $E_\pi(|\mathbf{p}|)$.

Q	m	$ \mathbf{p} =0$	$ \mathbf{p} =1$	$ \mathbf{p} =\sqrt{2}$	$ \mathbf{p} =\sqrt{3}$
0	0.015	0.1722(20)	0.4236(88)	0.554(27)	0.710(17)
0	0.025	0.2193(16)	0.4499(58)	0.5791(96)	0.694(16)
0	0.035	0.2610(15)	0.4706(33)	0.6091(59)	0.721(11)
0	0.050	0.3128(12)	0.5005(21)	0.6292(28)	0.732(11)
-2	0.050	0.3124(15)	0.4972(34)	0.6257(67)	0.738(14)
-4	0.050	0.3155(17)	0.4994(29)	0.6353(51)	0.705(10)

$F_V(\Delta t, \Delta t'; q^2)$. Examples of $F_V(\Delta t, \Delta t'; q^2)$ are plotted in Figs. 5 and 6. The all-to-all quark propagator enables us to change Δt and $\Delta t'$ independently in contrast to previous lattice studies

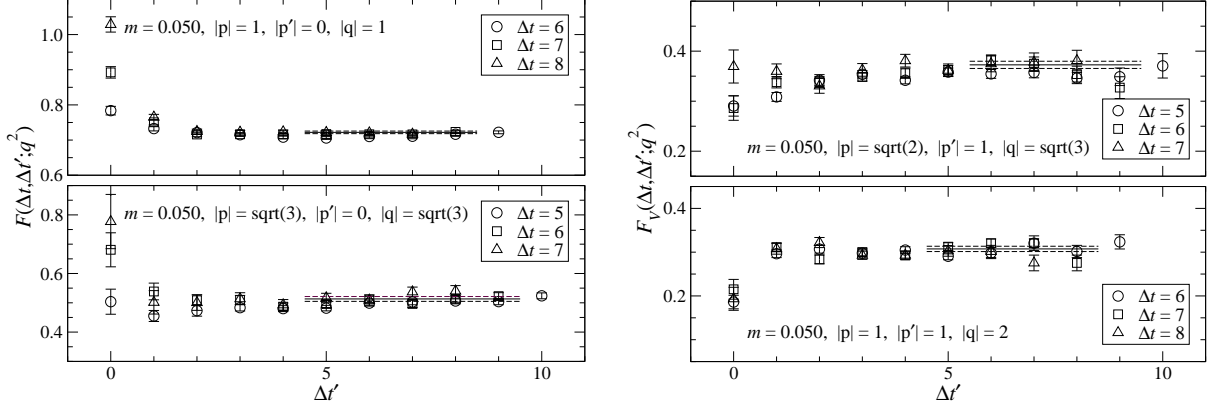


FIG. 5: Effective value of vector form factor $F_V(\Delta t, \Delta t'; q^2)$ at $(Q, m) = (0, 0.050)$. We only plot data with $\Delta t + \Delta t' < N_t/2$. Momenta written in the legends are spatial and in units of $2\pi a/L$.

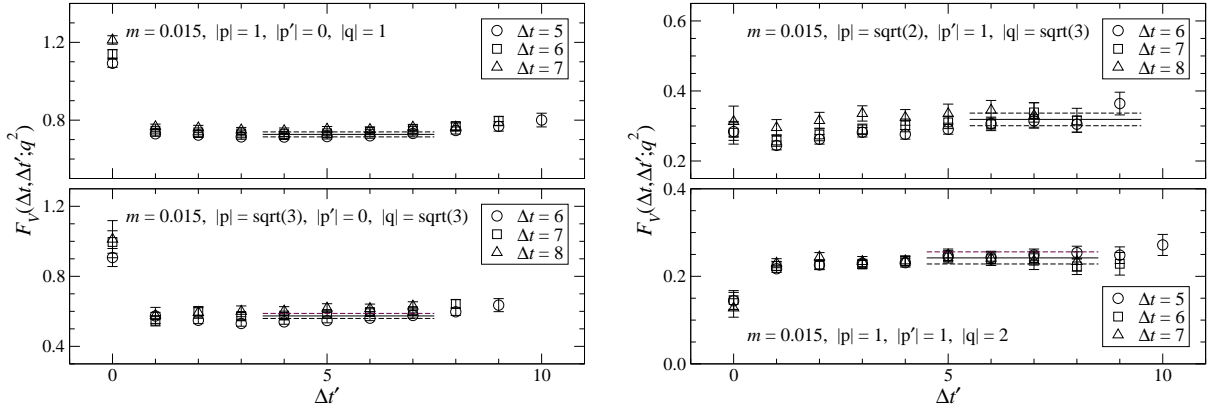


FIG. 6: Effective value of $F_V(\Delta t, \Delta t'; q^2)$ at $(Q, m) = (0, 0.015)$.

with the point-to-all propagator where their sum $\Delta t + \Delta t'$ is kept fixed. This is helpful to identify the plateau in $F_V(\Delta t, \Delta t'; q^2)$ as well as to stabilize the fit by increasing the number of available data. Fit results are summarized in Tables II–V. The statistical accuracy of $F_V(q^2)$ is typically 3–5 % at all of our simulated quark masses. Only the combination of our two largest momenta $(|\mathbf{p}|, |\mathbf{p}'|) = (\sqrt{3}, \sqrt{2})$ has larger statistical error of about 10 %. This is probably because precise determination of the ground state contribution is difficult due to very rapid damping of pion correlators with such large momenta.

TABLE II: Fit results for pion form factors at $(Q, m) = (0, 0.050)$.

$ \mathbf{p} $	$ \mathbf{p}' $	$ \mathbf{q} $	q^2	$F_V(q^2)$	$\frac{F_S(q^2)}{F_S(q_{\text{ref}}^2)}$	$ \mathbf{p} $	$ \mathbf{p}' $	$ \mathbf{q} $	q^2	$F_V(q^2)$	$\frac{F_S(q^2)}{F_S(q_{\text{ref}}^2)}$
0	0	0	0	1	1.30(11)	$\sqrt{3}$	0	$\sqrt{3}$	-0.2865(95)	0.5132(83)	0.705(44)
1	0	1	-0.1190(7)	0.7219(37)	-	$\sqrt{3}$	1	$\sqrt{2}$	-0.2546(51)	0.522(17)	0.728(66)
$\sqrt{2}$	1	1	-0.13763(68)	0.660(13)	0.918(37)	1	1	$\sqrt{2}$	-0.3084(0)	0.4755(47)	0.759(21)
$\sqrt{3}$	$\sqrt{2}$	1	-0.1436(23)	0.599(49)	0.907(90)	$\sqrt{2}$	1	$\sqrt{3}$	-0.4461(7)	0.3726(72)	0.681(34)
$\sqrt{2}$	0	$\sqrt{2}$	-0.2083(18)	0.5908(45)	0.871(17)	1	1	2	-0.6169(0)	0.3075(61)	0.605(33)

TABLE III: Fit results for pion form factors at $(Q, m) = (0, 0.035)$.

$ \mathbf{p} $	$ \mathbf{p}' $	$ \mathbf{q} $	q^2	$F_V(q^2)$	$\frac{F_S(q^2)}{F_S(q_{\text{ref}}^2)}$	$ \mathbf{p} $	$ \mathbf{p}' $	$ \mathbf{q} $	q^2	$F_V(q^2)$	$\frac{F_S(q^2)}{F_S(q_{\text{ref}}^2)}$
0	0	0	0	1	1.28(10)	$\sqrt{3}$	0	$\sqrt{3}$	-0.2513(99)	0.5266(98)	0.673(69)
1	0	1	-0.1103(15)	0.7272(65)	-	$\sqrt{3}$	1	$\sqrt{2}$	-0.2459(54)	0.513(25)	0.783(66)
$\sqrt{2}$	1	1	-0.1350(17)	0.638(18)	0.902(43)	1	1	$\sqrt{2}$	-0.3084(0)	0.4518(80)	0.765(27)
$\sqrt{3}$	$\sqrt{2}$	1	-0.1417(27)	0.610(85)	0.890(87)	$\sqrt{2}$	1	$\sqrt{3}$	-0.4435(17)	0.358(11)	0.648(53)
$\sqrt{2}$	0	$\sqrt{2}$	-0.1873(44)	0.5964(75)	0.728(64)	1	1	2	-0.6169(0)	0.2882(76)	0.546(31)

TABLE IV: Fit results for pion form factors at $(Q, m) = (0, 0.025)$.

$ \mathbf{p} $	$ \mathbf{p}' $	$ \mathbf{q} $	q^2	$F_V(q^2)$	$\frac{F_S(q^2)}{F_S(q_{\text{ref}}^2)}$	$ \mathbf{p} $	$ \mathbf{p}' $	$ \mathbf{q} $	q^2	$F_V(q^2)$	$\frac{F_S(q^2)}{F_S(q_{\text{ref}}^2)}$
0	0	0	0	1	1.29(13)	$\sqrt{3}$	0	$\sqrt{3}$	-0.237(15)	0.529(12)	0.650(35)
1	0	1	-0.1010(27)	0.7327(88)	-	$\sqrt{3}$	1	$\sqrt{2}$	-0.2489(83)	0.474(24)	0.56(11)
$\sqrt{2}$	1	1	-0.1375(27)	0.627(21)	0.939(61)	1	1	$\sqrt{2}$	-0.3084(0)	0.422(11)	0.686(42)
$\sqrt{3}$	$\sqrt{2}$	1	-0.1410(38)	0.550(60)	0.49(31)	$\sqrt{2}$	1	$\sqrt{3}$	-0.4460(27)	0.337(12)	0.548(50)
$\sqrt{2}$	0	$\sqrt{2}$	-0.1790(70)	0.600(10)	0.768(30)	1	1	2	-0.6169(0)	0.2561(87)	0.523(54)

TABLE V: Fit results for pion form factors at $(Q, m) = (0, 0.015)$.

$ \mathbf{p} $	$ \mathbf{p}' $	$ \mathbf{q} $	q^2	$F_V(q^2)$	$\frac{F_S(q^2)}{F_S(q_{\text{ref}}^2)}$	$ \mathbf{p} $	$ \mathbf{p}' $	$ \mathbf{q} $	q^2	$F_V(q^2)$	$\frac{F_S(q^2)}{F_S(q_{\text{ref}}^2)}$
0	0	0	0	1	1.29(19)	$\sqrt{3}$	0	$\sqrt{3}$	-0.174(18)	0.574(14)	0.621(90)
1	0	1	-0.0910(44)	0.727(13)	-	$\sqrt{3}$	1	$\sqrt{2}$	-0.227(11)	0.484(33)	0.80(12)
$\sqrt{2}$	1	1	-0.1372(73)	0.645(34)	0.926(86)	1	1	$\sqrt{2}$	-0.3084(0)	0.403(16)	0.643(95)
$\sqrt{3}$	$\sqrt{2}$	1	-0.1301(98)	0.629(74)	0.81(41)	$\sqrt{2}$	1	$\sqrt{3}$	-0.4456(73)	0.319(18)	0.599(81)
$\sqrt{2}$	0	$\sqrt{2}$	-0.162(21)	0.631(25)	0.805(44)	1	1	2	-0.6169(0)	0.242(14)	0.65(13)

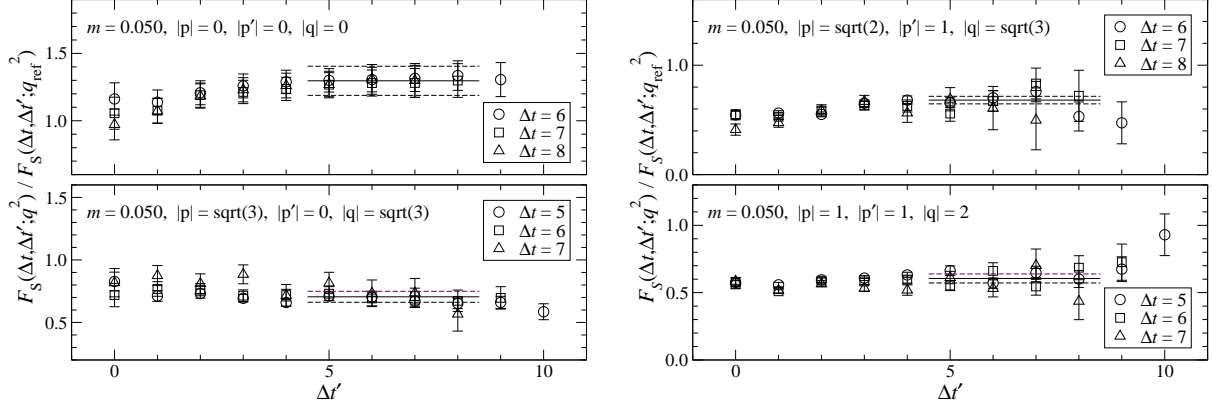


FIG. 7: Effective value of normalized scalar form factor $F_S(\Delta t, \Delta t'; q^2)/F_S(\Delta t, \Delta t'; q_{\text{ref}}^2)$ at $(Q, m) = (0, 0.050)$.

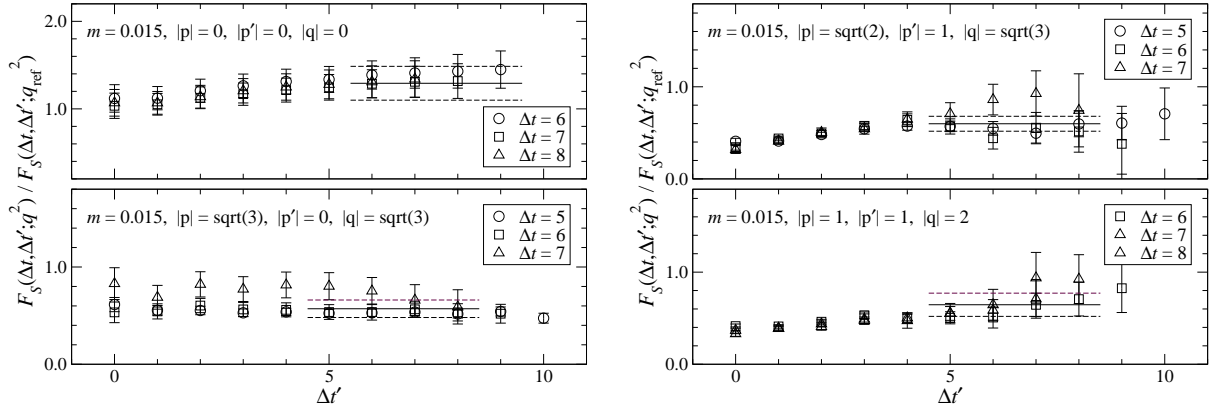


FIG. 8: Effective value of $F_S(\Delta t, \Delta t'; q^2)/F_S(\Delta t, \Delta t'; q_{\text{ref}}^2)$ at $(Q, m) = (0, 0.015)$.

B. Scalar form factor

The scalar form factor normalized by the value at a certain momentum transfer q_{ref}^2 can be calculated from the following ratio similar to that for $F_V(q^2)$

$$\frac{F_S(\Delta t, \Delta t'; q^2)}{F_S(\Delta t, \Delta t'; q_{\text{ref}}^2)} = \frac{R_S(\Delta t, \Delta t'; q^2)}{R_S(\Delta t, \Delta t'; q_{\text{ref}}^2)}, \quad (24)$$

$$R_S(\Delta t, \Delta t'; q^2) = \frac{1}{N_{|\mathbf{p}|, |\mathbf{p}'|}} \sum_{\text{fixed } |\mathbf{p}|, |\mathbf{p}'|} \frac{C_{\pi 1\pi}^{(\text{sngl})}(\Delta t, \Delta t'; \mathbf{p}, \mathbf{p}')}{C_{\pi\pi, \phi_s \phi_l}(\Delta t; \mathbf{p}) C_{\pi\pi, \phi_l \phi_s}(\Delta t'; \mathbf{p}')}, \quad (25)$$

where

$$C_{\pi 1\pi}^{(\text{sngl})}(\Delta t, \Delta t'; \mathbf{p}, \mathbf{p}') = C_{\pi 1\pi}^{(\text{conn})}(\Delta t, \Delta t'; \mathbf{p}, \mathbf{p}') - C_{\pi 1\pi}^{(\text{disc})}(\Delta t, \Delta t'; \mathbf{p}, \mathbf{p}') + C_{\pi 1\pi}^{(\text{vev})}(\Delta t, \Delta t'; \mathbf{p}, \mathbf{p}') \quad (26)$$

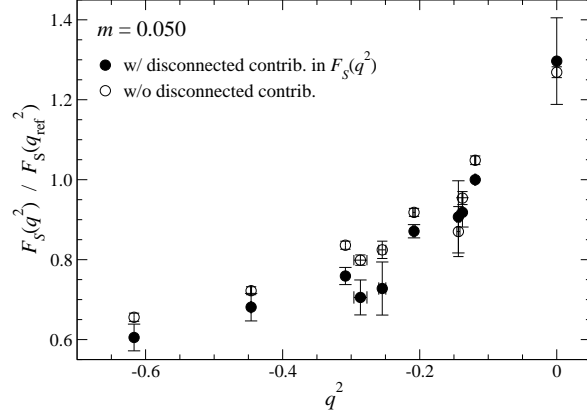


FIG. 9: Normalized scalar form factor $F_S(q^2)/F_S(q_{\text{ref}}^2)$ with and without the contributions of disconnected diagram to $F_S(q^2)$. We use the normalization value $F_S(q_{\text{ref}}^2)$ with the disconnected contributions in both data.

is the three-point function with the flavor-singlet scalar operator. We note that $C_{\pi 1\pi}^{(\text{disc})} - C_{\pi 1\pi}^{(\text{vev})}$ suffers from a severe cancellation: it is typically a subtraction of $O(1)$ quantities to extract their $O(10^{-3})$ difference. Although this subtraction leads to a large statistical error in $F_S(q^2)$, it is present only at $|\mathbf{q}| = 0$, since $C_{\pi 1\pi}^{(\text{vev})}$ vanishes at nonzero $|\mathbf{q}|$. In the following analysis, therefore, we use $F_S(q^2)$ normalized at the smallest nonzero $|q^2|$ with $|\mathbf{q}_{\text{ref}}| = 1$ rather than at $q^2 = 0$. The effective value of the normalized scalar form factor $F_S(\Delta t, \Delta t'; q^2)/F_S(\Delta t, \Delta t'; q_{\text{ref}}^2)$ is plotted in Figs. 7 and 8. We summarize $F_S(q^2)/F_S(q_{\text{ref}}^2)$ determined from a constant fit to $F_S(\Delta t, \Delta t'; q^2)/F_S(\Delta t, \Delta t'; q_{\text{ref}}^2)$ in Tables II–V.

Figure 9 compares $F_S(q^2)/F_S(q_{\text{ref}}^2)$ to that without the contributions of the disconnected diagrams to $F_S(q^2)$. We observe a small but significant deviation between the two data, which implies the importance of the disconnected contributions.

An accurate estimate of $F_S(0)$ is useful for a precise determination of the scalar radius $\langle r^2 \rangle_S$, as it characterizes the q^2 dependence of $F_S(q^2)$ near $q^2 = 0$. Since the extraction of $F_S(0)$ from the three-point function suffers from large statistical error due to the subtraction of the vacuum expectation value (VEV) of the scalar operator, we test an alternative calculation of $F_S(0)$ through the Feynman-Hellmann theorem

$$F_S(0) = \frac{1}{2} \frac{\partial M_\pi^2}{\partial m}, \quad (27)$$

where the VEV subtraction is implicitly taken into account. Note that the overall factor $1/2$ is present in the RHS, since m is the mass of two degenerate quark flavors. This and $F_S(q_{\text{ref}})$

TABLE VI: Scalar form factor $F_S(0)$ determined from Feynman-Hellmann theorem Eq. (27), and its value normalized by $F_S(q_{\text{ref}}^2)$ from ratio (28). The first error is statistical. The second is systematics due to the choice of the fit form for M_π^2 and uncertainty in Z_S .

m	0.015	0.025	0.035	0.050
$F_S(0)$	1.149(6)(22)	1.162(18)(37)	1.208(29)(47)	1.319(44)(52)
$F_S(0)/F_S(q_{\text{ref}}^2)$	1.413(70)(28)	1.415(44)(44)	1.338(38)(51)	1.441(53)(58)

determined from a ratio of pion correlators

$$F_S(q^2) \xleftarrow{\Delta t, \Delta t' \rightarrow \infty} 2Z_S E_\pi(|\mathbf{p}'|) \frac{C_{\pi 1\pi}^{(\text{sngl})}(\Delta t, \Delta t'; \mathbf{p}, \mathbf{p}') C_{\pi\pi, \phi_s \phi_l}(\Delta t'; \mathbf{p}')}{C_{\pi\pi, \phi_s \phi_l}(\Delta t; \mathbf{p}) C_{\pi\pi, \phi_s \phi_s}(\Delta t + \Delta t'; \mathbf{p}')} \quad (28)$$

provide an alternative estimate of the normalized form factor $F_S(0)/F_S(q_{\text{ref}}^2)$. We determine $F_S(0)$ from the chiral fit of M_π^2 and $Z_S = 0.838(14)(3)$ presented in Ref. [5]. Results for $F_S(0)$ and $F_S(0)/F_S(q_{\text{ref}}^2)$ are summarized in Table VI, where the systematic error is estimated by changing the fitting form for M_π^2 and by taking account of the uncertainty in Z_S . It turns out that, with the setup of our measurements, the Feynman-Hellmann theorem (27) leads to a slightly smaller uncertainty in $F_S(0)/F_S(q_{\text{ref}}^2)$ than that from the ratio (24). We therefore adopt $F_S(0)/F_S(q_{\text{ref}}^2)$ in Table VI and $F_S(q^2 \neq 0)/F_S(q_{\text{ref}}^2)$ in Tables II–V in the following analysis.

C. Finite volume correction

The finite volume effect could be significant at two smallest quark masses $m = 0.015$ and 0.025 , as the value of $M_\pi L$ is less than 4. We estimate the finite volume correction (FVC) to the pion mass as presented in Ref. [5]. The FVC to the vector form factor $F_V(q^2)$ has been calculated within one-loop ChPT in Refs. [45, 46] by replacing the loop integral by a discrete sum

$$\Delta F_V(q^2) = \frac{1}{2F^2} \int_0^1 dx \{ I_{1/2}(L, x\mathbf{q}, M_\pi^2 + x(1-x)q^2) - I_{1/2}(L, \mathbf{0}, M_\pi^2) \}, \quad (29)$$

where

$$I_s(L, \Delta\mathbf{k}, M^2) = \int \frac{d^3k}{(2\pi)^3} \frac{1}{\{(\mathbf{k} + \Delta\mathbf{k})^2 + M^2\}^s} - \frac{1}{L^3} \sum_{\mathbf{k}} \frac{1}{\{(\mathbf{k} + \Delta\mathbf{k})^2 + M^2\}^s}. \quad (30)$$

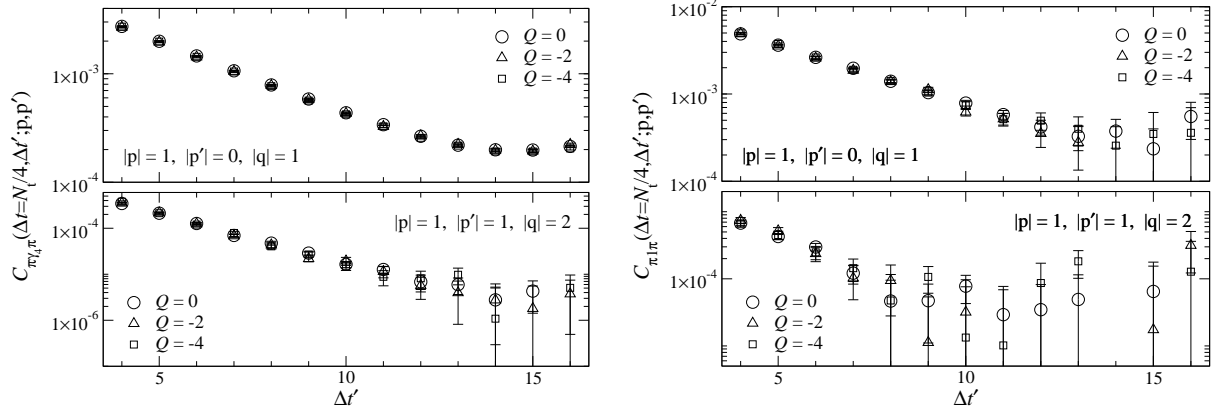


FIG. 10: Three-point functions with vector current (left panels) and scalar operator (right panels) calculated in different topological sectors for $m = 0.050$. Top and bottom panels show data at the smallest and largest nonzero $|q^2|$.

This function can be evaluated through the elliptic θ function [47, 48] as

$$I_s(L, \Delta \mathbf{k}, M^2) = \frac{1}{(4\pi)^{3/2} \Gamma(s)} \int_0^\infty d\tau \tau^{s-5/2} e^{-M^2 \tau} \left\{ 1 - \prod_{i=1}^3 \theta_3 \left(\frac{L}{2} \Delta k_i, e^{-L^2/4\tau} \right) \right\}, \quad (31)$$

$$\theta_3(u, q) = \sum_{n=-\infty}^{\infty} q^{n^2} e^{2nui}. \quad (32)$$

The FVC to the scalar form factor $F_S(q^2)$ is similarly evaluated as

$$\Delta F_S(q^2) = \frac{B}{2F^2} \int_0^1 dx \left\{ -\frac{2q^2 + M_\pi^2}{2} I_{3/2}(L, x\mathbf{q}, M_\pi^2 + x(1-x)q^2) + I_{1/2}(L, \mathbf{0}, M_\pi^2) \right\}, \quad (33)$$

where we use $B = 2.10(45)$ GeV obtained from our analysis of the pion mass [5]. We find that $\Delta F_V(q^2)$ has a mild q^2 dependence and its magnitude is similar to or smaller than the statistical error: it is typically 3–5 % at $m = 0.015$, and decreases down to $\lesssim 1$ % at $m = 0.050$. The FVC to the normalized scalar form factor $F_S(q^2)/F_S(q_{\text{ref}}^2)$ is below the statistical uncertainty even at our smallest quark mass due to a partial cancellation of FVCs in the ratio. We use $F_V(q^2)$ and $F_S(q^2)/F_S(q_{\text{ref}}^2)$ with the FVC included in the following analysis.

D. Fixed topology effects

The form factors listed in Tables II–V are extracted in the trivial topological sector, and are subject to effects of the fixed topology. The effects are known to be suppressed by the inverse space-time volume $1/V$ [37, 38], and are systematically correctable [38]. In order to confirm if the correction to our data is statistically insignificant, we repeat the calculation of $F_V(q^2)$ and $F_S(q^2)$

TABLE VII: Fit results for pion form factors at $(Q, m) = (-2, 0.050)$.

$ \mathbf{p} $	$ \mathbf{p}' $	$ \mathbf{q} $	q^2	$F_V(q^2)$	$\frac{F_S(q^2)}{F_S(q_{\text{ref}}^2)}$	$ \mathbf{p} $	$ \mathbf{p}' $	$ \mathbf{q} $	q^2	$F_V(q^2)$	$\frac{F_S(q^2)}{F_S(q_{\text{ref}}^2)}$
1	0	1	-0.1200(11)	0.7145(46)	-	$\sqrt{3}$	1	$\sqrt{2}$	-0.2503(70)	0.481(22)	0.79(13)
$\sqrt{2}$	1	1	-0.1377(15)	0.667(20)	0.923(51)	1	1	$\sqrt{2}$	-0.3084(0)	0.4640(65)	0.738(29)
$\sqrt{3}$	$\sqrt{2}$	1	-0.1416(33)	0.662(56)	0.32(34)	$\sqrt{2}$	1	$\sqrt{3}$	-0.4461(15)	0.365(11)	0.694(46)
$\sqrt{2}$	0	$\sqrt{2}$	-0.2102(40)	0.5910(75)	0.829(23)	1	1	2	-0.6169(0)	0.2962(89)	0.635(55)
$\sqrt{3}$	0	$\sqrt{3}$	-0.281(12)	0.5113(97)	0.785(65)	-	-	-	-	-	-

TABLE VIII: Fit results for pion form factors at $(Q, m) = (-4, 0.050)$.

$ \mathbf{p} $	$ \mathbf{p}' $	$ \mathbf{q} $	q^2	$F_V(q^2)$	$\frac{F_S(q^2)}{F_S(q_{\text{ref}}^2)}$	$ \mathbf{p} $	$ \mathbf{p}' $	$ \mathbf{q} $	q^2	$F_V(q^2)$	$\frac{F_S(q^2)}{F_S(q_{\text{ref}}^2)}$
1	0	1	-0.1204(9)	0.7234(58)	-	$\sqrt{3}$	1	$\sqrt{2}$	-0.2660(42)	0.561(22)	0.94(11)
$\sqrt{2}$	1	1	-0.1357(11)	0.641(21)	0.899(49)	1	1	$\sqrt{2}$	-0.3084(0)	0.4810(83)	0.846(29)
$\sqrt{3}$	$\sqrt{2}$	1	-0.1493(16)	0.699(76)	0.39(32)	$\sqrt{2}$	1	$\sqrt{3}$	-0.4442(11)	0.3714(96)	0.754(57)
$\sqrt{2}$	0	$\sqrt{2}$	-0.2062(29)	0.5875(48)	0.872(26)	1	1	2	-0.6169(0)	0.3143(86)	0.603(42)
$\sqrt{3}$	0	$\sqrt{3}$	-0.3107(78)	0.5392(87)	0.820(52)	-	-	-	-	-	-

in non-trivial topological sectors with $Q = -2$ and -4 at $m = 0.050$. Note that, LO ChPT predicts $\langle Q^2 \rangle = m\Sigma V/2 \sim 8$ with our estimate of the chiral condensate $\Sigma^{\overline{\text{MS}}}(2 \text{ GeV}) = (0.236^{+14}_{-5}) \text{ GeV}^3$ [5]. It is therefore not necessary to simulate topological sectors with $|Q| \gg \sqrt{\langle Q^2 \rangle} \sim 3$ at this quark mass.

We compare three-point functions calculated in the different topological sectors in Fig. 10, where no systematic deviation among the data is observed. This is also the case for $F_{V,S}(q^2)$ summarized in Tables VII and VIII. The form factors at $Q = 0, -2$ and -4 are consistent with each other within two standard deviations as shown in Fig. 11. Although the effect of the fixed topology is likely below our statistical accuracy, we take the spread in $F_{V,S}(q^2)$ as a systematic error at $m = 0.050$ and an uncertainty of the same magnitude is assumed at $m < 0.050$ in the following analysis.

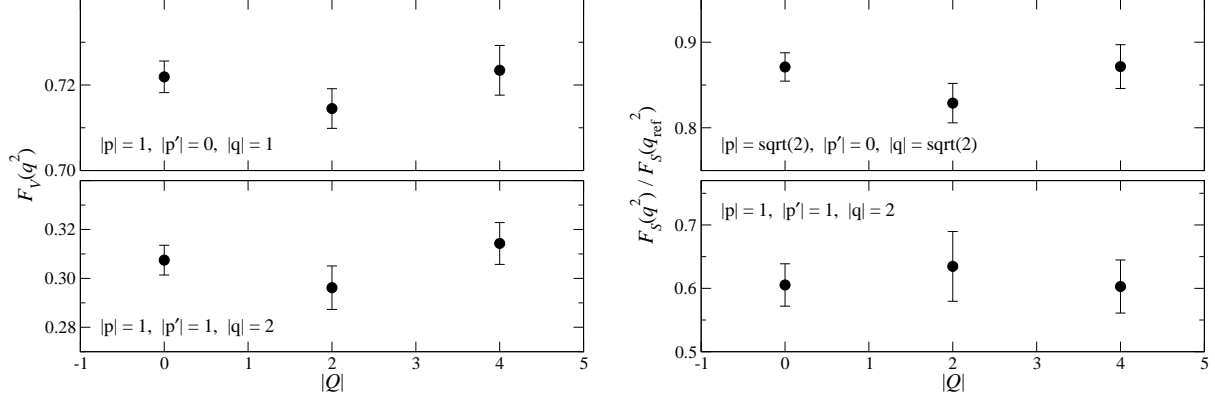


FIG. 11: Vector (left panels) and scalar form factors (right panels) calculated in different topological sectors for $m=0.050$.

IV. PARAMETRIZATION OF THE q^2 DEPENDENCE

A. Vector form factor

The vector form factor $F_V(q^2)$ is plotted as a function of q^2 in Fig. 12. Its q^2 dependence turns out to be close to the expectation from the vector meson dominance (VMD) hypothesis

$$F_V(q^2) = \frac{1}{1 - q^2/M_\rho^2}, \quad (34)$$

where M_ρ is the vector meson mass calculated at the same quark mass. Then, we assume that the small deviation due to higher poles or cuts can be well parametrized by a polynomial form. We therefore fit our data to the following form

$$F_V(q^2) = \frac{1}{1 - q^2/M_\rho^2} + a_{V,1} q^2 + a_{V,2} (q^2)^2 + a_{V,3} (q^2)^3 \quad (35)$$

in order to extract the charge radius $\langle r^2 \rangle_V$ and the curvature c_V

$$\langle r^2 \rangle_V = 6 \frac{\partial F_V(q^2)}{\partial (q^2)} \Big|_{q^2=0}, \quad c_V = \frac{\partial^2 F_V(q^2)}{\partial (q^2)^2} \Big|_{q^2=0}. \quad (36)$$

The fit curve is plotted in Fig. 12 and numerical results are summarized in Table IX. The fit describes our data reasonably well, and results for $\langle r^2 \rangle_V$ and c_V do not change significantly by including or excluding the cubic term $a_{V,3}(q^2)^3$. In the following analysis, we employ results from the parametrization with the cubic term.

One of the main purposes of this work is to investigate whether the q^2 dependence of our data can be described by two-loop ChPT [15, 16]. Figure 13 shows contributions to $F_V(q^2)$ from each order $(q^2)^n$ of a Taylor expansion of Eq. (35). We find that $O(q^6)$ and higher order contributions

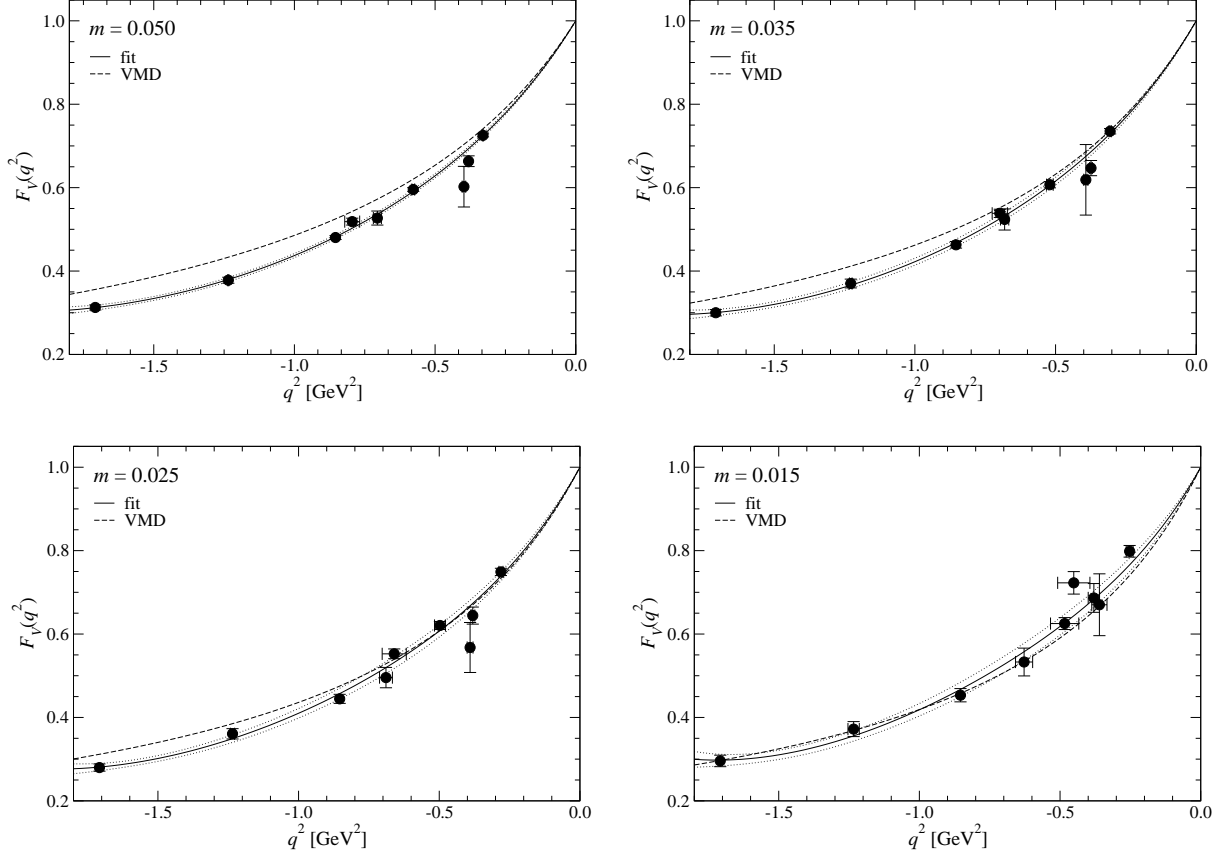


FIG. 12: Vector form factor $F_V(q^2)$ as a function of q^2 . Solid and dotted lines show the fit curve (35) and its error. The q^2 dependence from the vector meson dominance model is shown by the dashed line.

TABLE IX: Parametrization Eq. (35) for vector form factor $F_V(q^2)$. Results for the vector radius $\langle r^2 \rangle_V$ and curvature c_V in lattice units are also listed.

m	$\chi^2/\text{d.o.f.}$	$a_{V,1}$	$a_{V,2}$	$a_{V,3}$	$\langle r^2 \rangle_V$	c_V
0.050	1.8(0.8)	0.187(33)	0.181(55)	—	18.72(20)	8.786(55)
0.050	1.7(0.9)	0.116(64)	-0.22(26)	-0.48(28)	18.30(38)	8.38(26)
0.035	1.3(0.5)	0.136(60)	0.124(96)	—	20.15(36)	10.51(10)
0.035	1.2(0.7)	0.02(11)	-0.50(44)	-0.73(46)	19.48(66)	9.88(44)
0.025	1.9(0.6)	0.034(90)	-0.03(14)	—	21.69(54)	12.78(14)
0.025	1.7(0.7)	-0.14(16)	-0.98(59)	-1.10(56)	20.64(98)	11.83(59)
0.015	0.8(0.8)	-0.09(12)	-0.15(19)	—	22.51(72)	14.58(19)
0.015	0.5(0.8)	-0.35(25)	-1.56(96)	-1.60(95)	20.9(1.5)	13.18(96)

to $F_V(q^2)$ are sufficiently small only below $|q^2| \simeq 0.3 \text{ GeV}^2$, which is however around our smallest value of $|q^2|$. We therefore do not use the parametrization based on ChPT in this study. Note

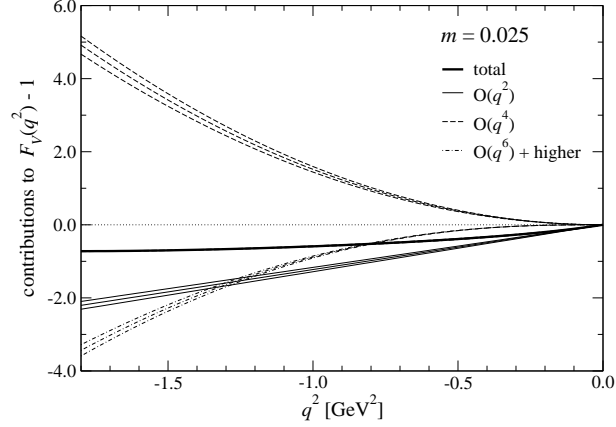


FIG. 13: Contributions in the q^2 expansion of $F_V(q^2)-1$ at $m=0.025$. Thin solid, dashed and dot-dashed lines show $O(q^2)$, $O(q^4)$ and higher contributions, whereas the thick solid line is their total.

TABLE X: Single pole fit (37). We also list the ρ meson mass at simulated quark masses.

m	$\chi^2/\text{d.o.f.}$	M_{pole}	$\langle r^2 \rangle_V$	c_V	M_ρ
0.050	4.3(1.1)	0.5431(50)	20.34(38)	11.49(43)	0.5839(28)
0.035	2.3(0.7)	0.5270(80)	21.61(65)	12.97(78)	0.5570(31)
0.025	2.9(0.8)	0.511(11)	23.0(1.0)	14.6(1.3)	0.5285(43)
0.015	0.7(0.7)	0.520(16)	22.2(1.4)	13.7(1.7)	0.5104(55)

that such large higher order contributions are unavoidable unless $|q^2| \ll M_\rho^2$, because the VMD form is a good approximation of $F_V(q^2)$.

We also test a single pole ansatz often used in the previous studies

$$F_V(q^2) = \frac{1}{1 - q^2/M_{\text{pole}}^2}. \quad (37)$$

As summarized in Table X, this fit tends to give a slightly higher χ^2 and $\langle r^2 \rangle_V$ than those from Eq. (35). This may suggest that it is difficult to describe our precise data of $F_V(q^2)$ in the whole region of $q^2[\text{GeV}^2] \in [-1.7, 0]$ by a simple pole-dominance form.

B. Scalar form factor

Due to the lack of knowledge about the scalar resonances at the simulated quark masses, we test a generic polynomial form up to the quartic order

$$F_S(q^2) = F_S(0) \{1 + a_{S,1} q^2 + a_{S,2} (q^2)^2 + a_{S,3} (q^2)^3 + a_{S,4} (q^2)^4\} \quad (38)$$

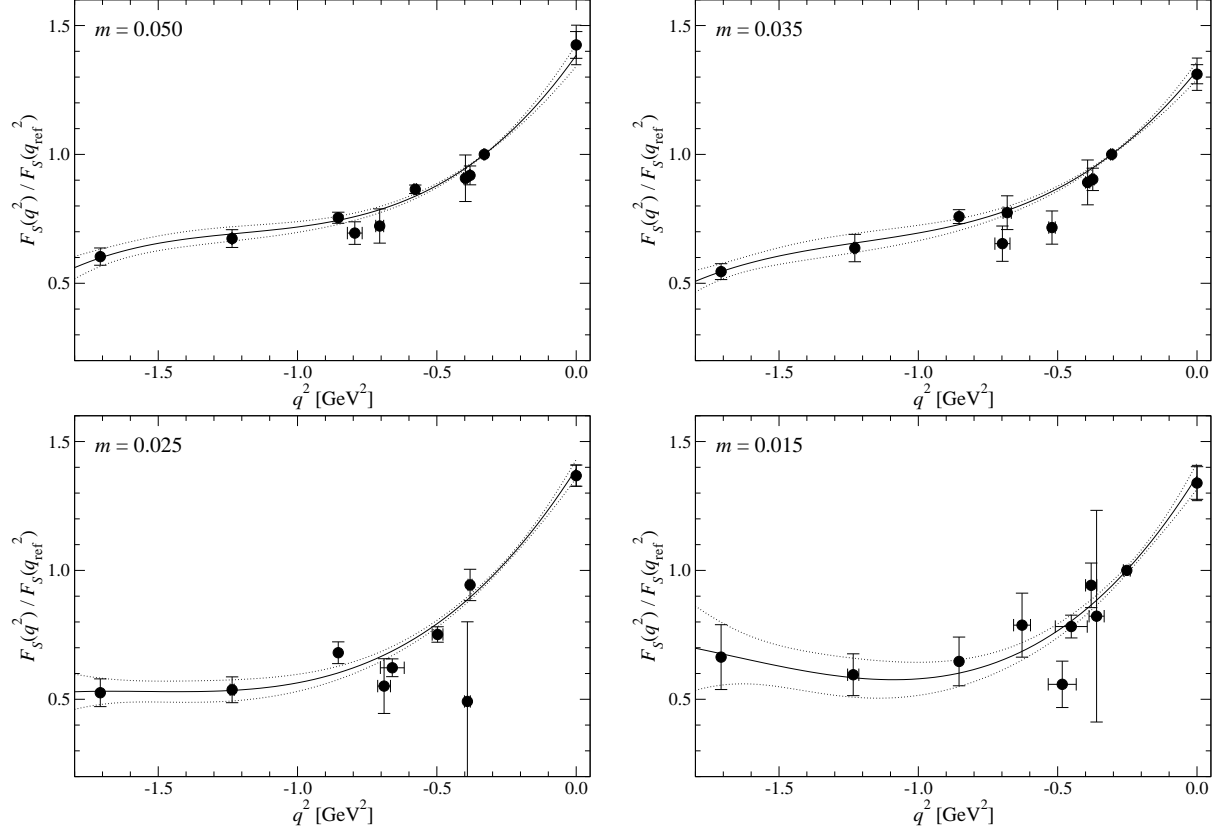


FIG. 14: Normalized scalar form factor $F_S(q^2)/F_S(q_{\text{ref}}^2)$ as a function of q^2 . Solid and dotted lines show the cubic fit and its error.

TABLE XI: Parametrization Eq. (38) for scalar form factor $F_S(q^2)$. Results for the vector radius $\langle r^2 \rangle_S$ and curvature c_S in lattice units are also listed.

m	$\chi^2/\text{d.o.f.}$	$a_{S,1}$	$a_{S,2}$	$a_{S,3}$	$a_{S,4}$	$\langle r^2 \rangle_S$	c_S
0.050	1.3(1.0)	3.04(31)	6.6(1.3)	5.1(1.4)	—	18.2(1.9)	6.6(1.3)
0.050	1.3(1.1)	3.51(49)	10.5(3.5)	1.6(9.2)	9.6(7.7)	21.1(3.0)	10.5(3.5)
0.035	1.8(1.0)	2.79(31)	5.6(1.4)	4.3(1.6)	—	16.8(1.9)	5.6(1.4)
0.035	1.9(1.2)	2.60(51)	3.5(4.8)	-3(15)	-6(13)	15.6(3.1)	3.5(4.8)
0.025	1.9(1.1)	3.37(32)	6.1(1.6)	3.6(1.8)	—	20.2(1.9)	6.1(1.6)
0.025	1.9(1.3)	2.97(53)	1.8(4.6)	-9(13)	-12(11)	17.8(3.2)	1.8(4.6)
0.015	1.5(1.0)	3.51(51)	6.6(2.7)	3.6(3.3)	—	21.0(3.1)	6.6(2.7)
0.015	1.7(1.1)	3.0(1.0)	1.0(9.1)	-14(26)	-16(22)	18.1(6.0)	1.0(9.1)

to parametrize the q^2 dependence of the scalar form factor $F_S(q^2)$. We observe that the cubic ($a_{S,4}=0$) fit also describes our data reasonably well as seen in Fig. 14. Fit results summarized in Table XI show that the inclusion of the quartic correction does not change the value of χ^2

and the result for the scalar radius $\langle r^2 \rangle_S = 6 a_{S,1}$ significantly. However, such a stability against the choice of the parametrization is much less clear in the curvature $c_S = a_{S,2}$ due to its large uncertainty. From these observations, we only use results for $\langle r^2 \rangle_S$ in the following analysis, and leave a precise determination of c_S for future studies.

V. CHIRAL EXTRAPOLATION

A. Fit based on one-loop ChPT

Since the form factors $F_{V,S}(q^2)$ are independent of q^2 at LO in ChPT, the chiral expansion of the radii $\langle r^2 \rangle_{V,S}$ starts from the one-loop order of ChPT. We first compare our lattice results with the one-loop expressions [14]

$$\langle r^2 \rangle_V = -\frac{1}{NF^2} (1 + 6N l_6^r) - \frac{1}{NF^2} \ln \left[\frac{M_\pi^2}{\mu^2} \right], \quad (39)$$

$$\langle r^2 \rangle_S = \frac{1}{NF^2} \left(-\frac{13}{2} + 6N l_4^r \right) - \frac{6}{NF^2} \ln \left[\frac{M_\pi^2}{\mu^2} \right], \quad (40)$$

where $N = (4\pi)^2$, and F is the decay constant in the chiral limit. We adopt the normalization of the decay constant $F_\pi = 92$ MeV at the physical quark mass. The renormalization scale μ is set to $4\pi F$ in our analysis. At this order of the chiral expansion, F is the only LEC appearing in the M_π dependent terms. We fix this important parameter to $F = 79.0(^{+5.0}_{-2.6})$ MeV, which has been determined from our detailed analysis of the pion mass and decay constant [5]. Each one of Eqs. (39) and (40), therefore, has a single fit parameter, namely LECs l_6^r or l_4^r in their constant term.

We find that the NLO fits of lattice data are not quite successful as seen in Fig. 15 and Table XII. While the data of $\langle r^2 \rangle_V$ can be fitted with reasonable $\chi^2/\text{d.o.f.} \sim 0.14$, the value extrapolated to the physical quark mass $\langle r^2 \rangle_V = 0.3637(43)$ fm² is significantly smaller than the experimental value $0.437(16)$ fm² based on $N_f = 2$ ChPT [16] and $0.452(11)$ fm² quoted by PDG [49]. As for the scalar radius, the one-loop formula fails to reproduce our data of $\langle r^2 \rangle_S$ as indicated by the quite large value of $\chi^2/\text{d.o.f.} \sim 9$: the data have a mild quark mass dependence in contrast to the 6 times enhanced chiral logarithm compared to $\langle r^2 \rangle_V$.

This failure of the NLO fits is not due to our choice of F . If F is treated as a free parameter, the fit to $\langle r^2 \rangle_S$ results in an unacceptably large value $F \simeq 200$ MeV to achieve reasonable $\chi^2/\text{d.o.f.} \lesssim 1$, whereas our data of $\langle r^2 \rangle_V$ favor $F \sim 80$ MeV. Thus we can not make a consistent

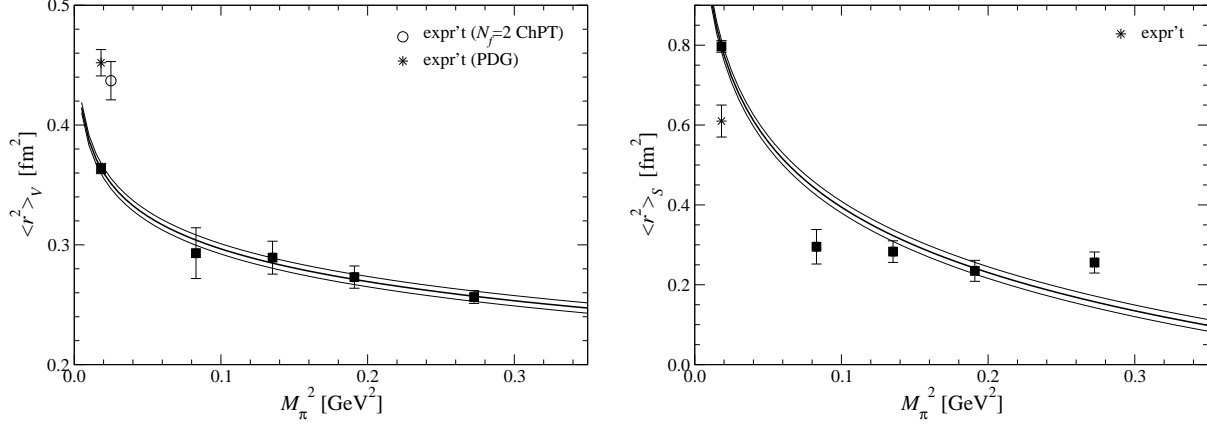


FIG. 15: Chiral fit of $\langle r^2 \rangle_V$ (left panel) and $\langle r^2 \rangle_S$ (right panel) using one-loop ChPT formulae. Filled squares are the lattice data and the value extrapolated to the physical point. In the left panel, we also plot the experimental value $\langle r^2 \rangle_V = 0.437(16)$ fm² from an analysis based on $N_f = 2$ ChPT [16] (open circle) and $0.452(11)$ fm² quoted by Particle Data Group [49] (star). The star symbol in the right panel represents $\langle r^2 \rangle_S = 0.61(4)$ fm² obtained from an indirect determination through $\pi\pi$ scattering [50].

TABLE XII: Results of chiral extrapolations of $\langle r^2 \rangle_V$ and $\langle r^2 \rangle_S$ using one-loop ChPT formulae Eqs. (39) and (40). The radii extrapolated to the physical point are also listed.

$\chi^2/\text{d.o.f.}$	$l_6^r \times 10^3$	$\langle r^2 \rangle_V [\text{fm}^2]$	$\chi^2/\text{d.o.f.}$	$l_4^r \times 10^3$	$\langle r^2 \rangle_S [\text{fm}^2]$
0.14	-6.59(12)	0.3637(43)	9.0	2.94(39)	0.797(15)

analysis. We note that we have experienced a similar situation, namely $\langle r^2 \rangle_V$ smaller than experiment and a small quark mass dependence of $\langle r^2 \rangle_S$, in our previous study with a different lattice action [23], though simulated quark masses are heavier than those in this study.

We also note that the lattice data for the curvature c_V largely deviate from its NLO ChPT expression as shown below. From all of these observations we conclude that the chiral behavior of the pion form factors in the quark mass region $m_s/6 - m_s/2$ are not well described by NLO ChPT.

B. Fit based on two-loop ChPT

In Ref. [5], we observed that NNLO contributions are important to reliably extract LECs from the pion mass and decay constant in our simulated region of the quark mass. Therefore there exists a possibility that NNLO contributions become also important to describe the chiral

TABLE XIII: Phenomenological estimates of LECs used in this paper. We note that $O(p^6)$ couplings $r_{\{V,S\},\{r,c\}}^r$ are based on a resonance saturation hypothesis.

Ref.[51]	Ref.[50]			Ref.[14]	Ref.[16]			
$F[\text{MeV}]$	\bar{l}_1	\bar{l}_2	\bar{l}_4	\bar{l}_3	\bar{l}_6	$r_{V,r}^r \times 10^4$	$r_{V,c}^r \times 10^4$	$r_{S,r}^r \times 10^4$
86.2(5)	-0.36(59)	4.31(11)	4.39(22)	2.9(2.4)	16.0(9)	-2.5	2.6	-0.3

behaviour of the radii. The two-loop expressions of $\langle r^2 \rangle_{V,S}$ and c_V are given by [15, 16]

$$\begin{aligned} \langle r^2 \rangle_V = & -\frac{1}{NF^2} (1 + 6N l_6^r) - \frac{1}{NF^2} \ln \left[\frac{M_\pi^2}{\mu^2} \right] \\ & + \frac{1}{N^2 F^4} \left(\frac{13N}{192} - \frac{181}{48} + 6N^2 r_{V,r}^r \right) M_\pi^2 + \frac{1}{N^2 F^4} \left(\frac{19}{6} - 12N l_{1,2}^r \right) M_\pi^2 \ln \left[\frac{M_\pi^2}{\mu^2} \right], \quad (41) \end{aligned}$$

$$\begin{aligned} \langle r^2 \rangle_S = & \frac{1}{NF^2} \left(-\frac{13}{2} + 6N l_4^r \right) - \frac{6}{NF^2} \ln \left[\frac{M_\pi^2}{\mu^2} \right] \\ & + \frac{1}{N^2 F^4} \left(-\frac{23N}{192} + \frac{869}{108} + 88N l_{1,2}^r + 80N l_2^r + 5N l_3^r - 24N^2 l_3^r l_4^r + 6N^2 r_{S,r}^r \right) M_\pi^2 \\ & + \frac{1}{N^2 F^4} \left(-\frac{323}{36} + 124N l_{1,2}^r + 130N l_2^r \right) M_\pi^2 \ln \left[\frac{M_\pi^2}{\mu^2} \right] - \frac{65}{3N^2 F^4} M_\pi^2 \ln \left[\frac{M_\pi^2}{\mu^2} \right]^2, \quad (42) \end{aligned}$$

$$\begin{aligned} c_V = & \frac{1}{60NF^2} \frac{1}{M_\pi^2} + \frac{1}{N^2 F^4} \left(\frac{N}{720} - \frac{8429}{25920} + \frac{N}{3} l_{1,2}^r + \frac{N}{6} l_6^r + N^2 r_{V,c}^r \right) \\ & + \frac{1}{N^2 F^4} \left(\frac{1}{108} + \frac{N}{3} l_{1,2}^r + \frac{N}{6} l_6^r \right) \ln \left[\frac{M_\pi^2}{\mu^2} \right] + \frac{1}{72N^2 F^4} \ln \left[\frac{M_\pi^2}{\mu^2} \right]^2, \quad (43) \end{aligned}$$

where we use a linear combination $l_{1,2}^r = l_1^r - l_2^r/2$ instead of l_1^r , since the former is convenient for our chiral extrapolation (see below). The analytic terms containing $r_{\{V,S\},\{r,c\}}^r$ represent contributions of tree diagrams with vertices from the $O(p^6)$ chiral Lagrangian.

Before fitting lattice data to these expressions, one can get some idea about the significance of the NNLO contributions by using phenomenological estimates of LECs. A collection of recent estimates is shown in Table XIII, where the LECs in the $O(p^4)$ chiral Lagrangian are denoted by the scale invariant convention \bar{l}_i defined by

$$l_i^r = \frac{\gamma_i}{2N} \left(\bar{l}_i + \ln \left[\frac{M_\pi^2}{\mu^2} \right] \right) \quad (44)$$

with

$$\gamma_1 = \frac{1}{3}, \quad \gamma_2 = \frac{2}{3}, \quad \gamma_3 = -\frac{1}{2}, \quad \gamma_4 = 2, \quad \gamma_6 = -\frac{1}{3}. \quad (45)$$

Figure 16 shows the expected M_π^2 dependence of $\langle r^2 \rangle_V$ and $\langle r^2 \rangle_S$ from Eqs. (41) and (42) with the phenomenological estimates of LECs. The individual contributions from NLO and NNLO are

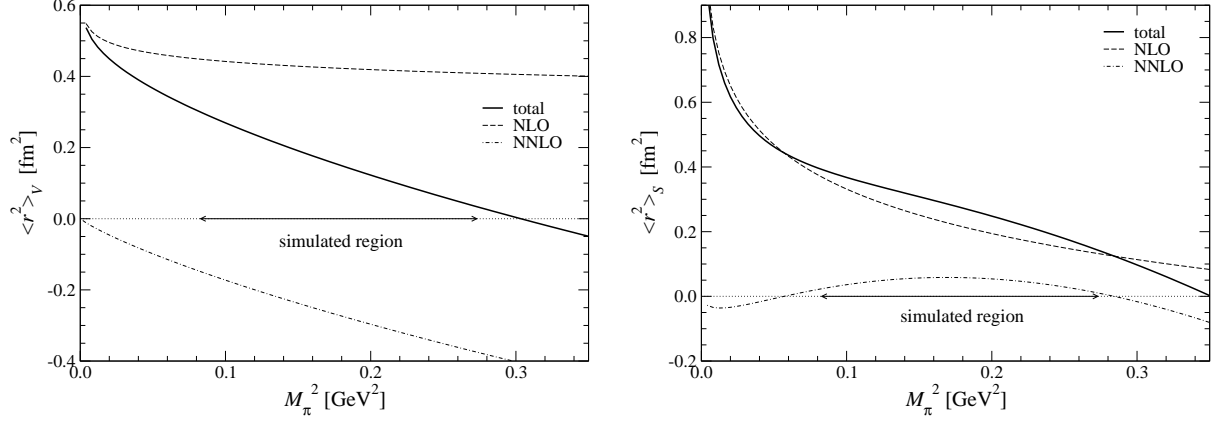


FIG. 16: Chiral behavior of radii based on two-loop ChPT with phenomenological estimates of LECs listed in Table XIII. The dashed and dot-dashed lines represent contributions at NLO and NNLO, whereas the solid line is their total. We note that $r_{\{V,S\},\{r,c\}}^r$ from the resonance saturation are taken as the renormalized LECs at the resonance mass scale in this plot.

also plotted. This analysis suggests that the NNLO contributions could significantly modify the chiral behavior of the radii in our simulated quark masses. However, we note that $r_{\{V,S\},\{r,c\}}^r$ are poorly known and these in Table XIII are determined from a resonance saturation hypothesis. A chiral extrapolation of lattice data with the two-loop formulae is therefore important to confirm the significance of the NNLO contributions and to resolve the failure of the one-loop fit.

The curvature c_V characterizes the $O(q^4)$ dependence of $F_V(q^2)$, and therefore requires the NNLO terms to describe its logarithmic dependence on the quark mass as well as a constant term. Near the chiral limit it has a divergent term of the form $\sim 1/(F^2 M_\pi^2)$, which comes from non-analytic NLO contributions in $F_V(q^2)$. Since the divergent term $1/(F^2 M_\pi^2)$ is significant only below the physical pion mass, the analysis of the lattice data for c_V requires the NNLO contributions.

We extend our analysis to two-loop ChPT as already outlined in our previous report [28]. The curvature c_V is included into our chiral extrapolation to obtain an additional constraint on LECs. Both of $\langle r^2 \rangle_V$ and c_V depend on l_1^r and l_2^r only through the linear combination $l_{1,2}^r$, and the complicated two-loop expressions for $\langle r^2 \rangle_V$ and c_V involve only four free parameters l_6^r , $l_{1,2}^r$, $r_{V,r}^r$ and $r_{V,c}^r$ by choosing $M_\pi^2/(4\pi F)^2$ as an expansion parameter. Therefore we first try a simultaneous fit to $\langle r^2 \rangle_V$ and c_V to check that the chiral behavior of our data is described by two-loop ChPT. Fit curves are plotted in Fig. 17 and numerical results are summarized in Table XIV. The fit leads to an acceptable value of $\chi^2/\text{d.o.f.} \sim 0.7$, and the relevant LECs are determined with a reasonable accuracy. We note that this fit is based only on ChPT without

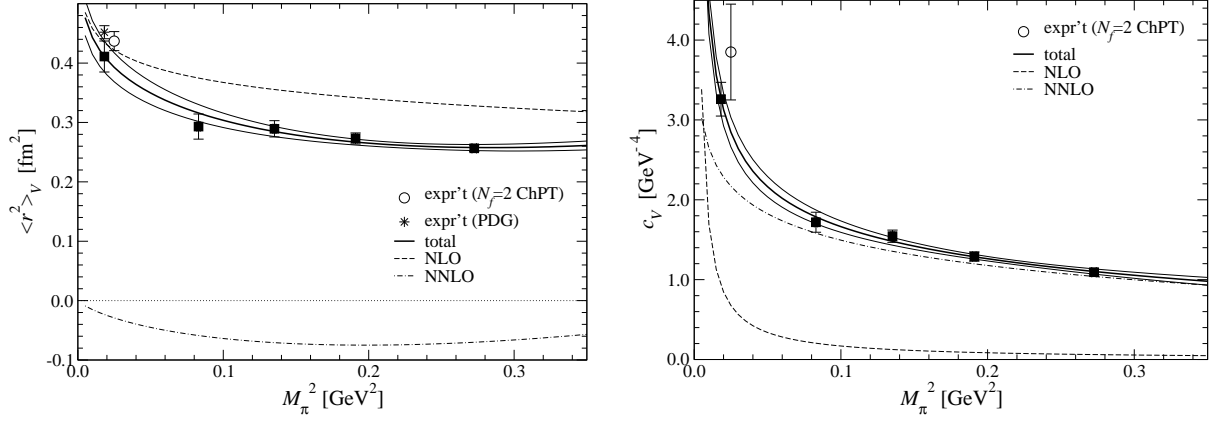


FIG. 17: Simultaneous chiral fit to $\langle r^2 \rangle_V$ and c_V based on two-loop formulae Eqs. (41) and (43). The experimental value for $c_V = 3.85(0.60)$ is taken from Ref. [16].

TABLE XIV: Results of simultaneous chiral fit to $\langle r^2 \rangle_V$ and c_V based on two-loop formulae Eqs. (41) and (43).

$\chi^2/\text{d.o.f.}$	$l_6^r \times 10^3$	$l_{12}^r \times 10^3$	$r_{V,r}^r \times 10^5$	$r_{V,c}^r \times 10^5$	$\langle r^2 \rangle_V [\text{fm}^2]$	$c_V [\text{GeV}^{-4}]$
0.70	-8.48(87)	-3.3(1.1)	-0.77(69)	3.97(20)	0.411(26)	3.26(21)

additional assumptions. The extrapolated values of $\langle r^2 \rangle_V$ and c_V are consistent with recent phenomenological determinations using experimental data of $F_V(q^2)$ [16, 52, 53, 54].

In Sec. IV, we observe that the $O(q^6)$ contribution to $F_V(q^2)$ is not small in the simulated region of the momentum transfer $q^2 \gtrsim 0.3 \text{ GeV}^2$ ($q^2/(4\pi F)^2 \gtrsim 0.3$). The q^2 dependence of our data is therefore parametrized by the generic polynomial forms (35) and (38) instead of those based on ChPT. This is not in contradiction with the successful chiral extrapolation of $\langle r^2 \rangle_V$ and c_V : since we explore small pion masses $M_\pi^2 \lesssim 0.3 \text{ GeV}^2$ ($M_\pi^2/(4\pi F)^2 \lesssim 0.3$), the quark mass dependence of $\langle r^2 \rangle_V$ and c_V is described by the two-loop ChPT formulae.

The inclusion of $\langle r^2 \rangle_S$ into the simultaneous chiral fit introduces additional four free parameters l_2^r , l_3^r , l_4^r and $r_{S,r}^r$, and we need to fix some of them to obtain a stable fit. Since l_2^r and l_3^r appear only in the NNLO terms and have been determined with a reasonable accuracy from phenomenology or lattice studies, we use a phenomenological estimate $\bar{l}_2 = 4.31(11)$ [50] and a lattice estimate $\bar{l}_3 = 3.38(56)$ from our analysis of the pion spectroscopy [5]. We treat $r_{S,r}^r$ and l_4^r as free parameters because of poor knowledge on the former and in order to examine the consistency of the latter with that determined from F_π . The fit curves are shown in Fig. 18 and numerical results are summarized in Table XV. We observe that i) the results in the vector

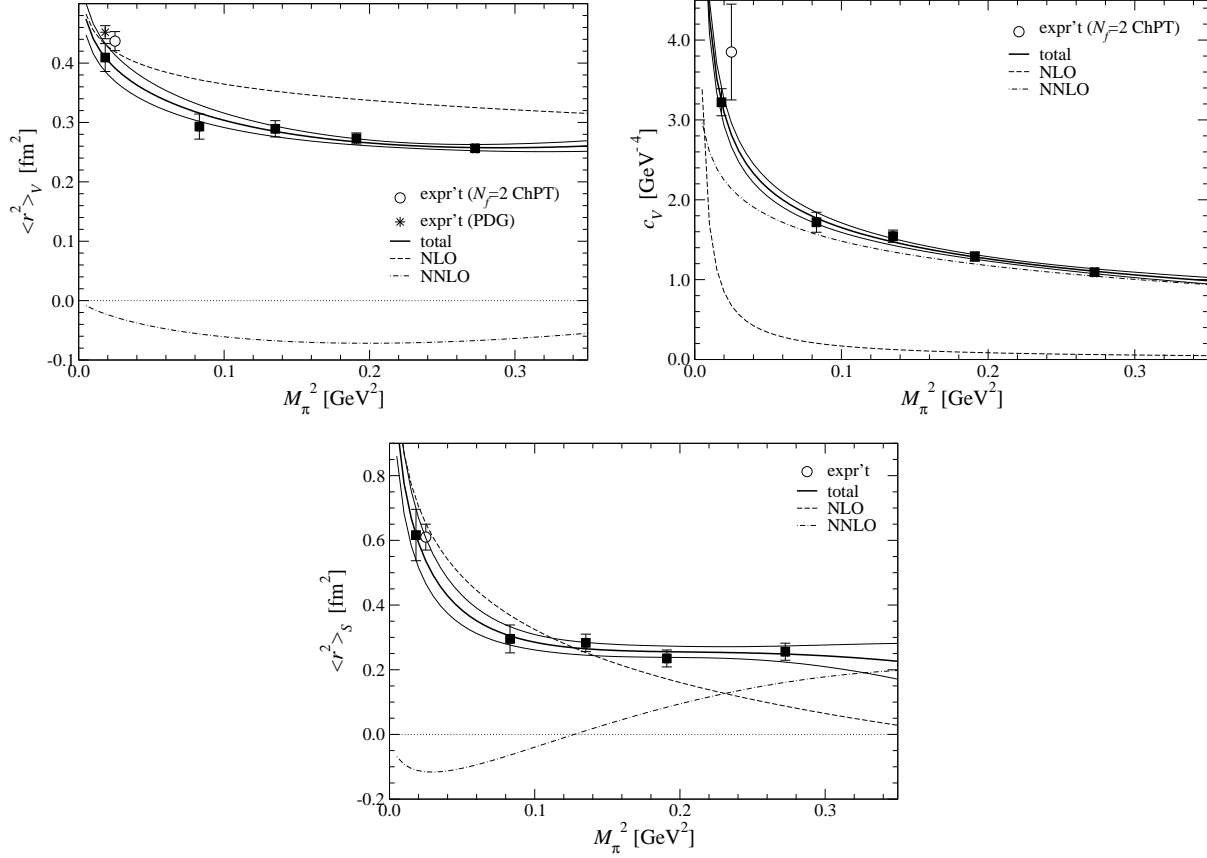


FIG. 18: Simultaneous chiral fit for radii $\langle r^2 \rangle_{V,S}$ and curvature c_V .

TABLE XV: Results of simultaneous chiral fit to $\langle r^2 \rangle_{V,S}$ and c_V based on two-loop formulae Eqs. (41), (42) and (43).

$\chi^2/\text{d.o.f.}$	$l_6^r \times 10^3$	$l_4^r \times 10^3$	$l_{1,2}^r \times 10^3$	$r_{V,r}^r \times 10^5$	$r_{V,c}^r \times 10^5$	$r_{S,r}^r \times 10^4$	$\langle r^2 \rangle_V [\text{fm}^2]$	$c_V [\text{GeV}^{-4}]$	$\langle r^2 \rangle_S [\text{fm}^2]$
0.68	-8.41(76)	1.1(3.2)	-3.10(90)	-1.0(1.1)	4.00(17)	1.74(36)	0.409(23)	3.22(17)	0.617(79)

channel, namely $\langle r^2 \rangle_V$, c_V and the relevant LECs, do not change significantly by including $\langle r^2 \rangle_S$ into the chiral fit, and ii) this fit describes the mild quark mass dependence of $\langle r^2 \rangle_S$ with an acceptable value of $\chi^2/\text{d.o.f.} \sim 0.7$. From Fig. 18, we find that the net NNLO contribution to $\langle r^2 \rangle_S$ is larger than NLO around our largest quark mass. This is due to an accidental cancellation between the constant and logarithmic terms at NLO.

We take results from this simultaneous fit as our best estimate of $\langle r^2 \rangle_{V,S}$, c_V . The systematic error due to the chiral extrapolation is estimated by excluding the data at the largest quark mass from the fit. The shifts in the radii and curvature turn out to be at the 1σ level: namely, the extrapolation is stable against variation of the fit range. In order to estimate systematics due to the fixed topology and the use of the Feynman-Hellmann theorem to estimate $F_S(0)$, we

TABLE XVI: Statistical and systematic errors of radii and curvature. We list the magnitude of the errors relative to the central values.

	stat.	sys.(total)	chiral fit	input(LECs)	input(r_0)	fixed Q	Feynman-Hellmann	finite a
$\langle r^2 \rangle_V$	6 %	9 %	5.3 %	0.2 %	6.1 %	2.2 %	1.4 %	3.0 %
$\langle r^2 \rangle_S$	13 %	11 %	4.0 %	2.2 %	7.7 %	2.4 %	4.6 %	3.0 %
c_V	5 %	11 %	2.7 %	0.4 %	9.3 %	2.3 %	3.8 %	3.0 %

repeat the whole analysis by using $F_{V,S}(q^2)$ shifted by their systematic uncertainties discussed in Secs. IIIB and IIID. Systematic uncertainties due to the choice of the inputs, namely LECs F , l_2^r , l_3^r for the chiral extrapolation and $r_0=0.49$ fm to fix the scale, are estimated by shifting each LEC by its uncertainty and by using a recent lattice estimate $r_0=0.47$ fm [55, 56]. In addition, a discretization error estimated by a naive order counting $O((a\Lambda_{\text{QCD}})^2) \approx 3\%$ is also taken into account. The magnitude of these systematic uncertainties are summarized in Table XVI. Our final results for the radii and curvature at the physical point are

$$\langle r^2 \rangle_V = 0.409(23)(37) \text{ fm}^2, \quad (46)$$

$$\langle r^2 \rangle_S = 0.617(79)(66) \text{ fm}^2, \quad (47)$$

$$c_V = 3.22(17)(36) \text{ GeV}^{-4}, \quad (48)$$

where the first error is statistical and the second represents systematic errors added in quadrature. These results are in good agreement with their phenomenological values. The largest systematic error arises from the use of the input r_0 to fix the scale. This can be removed by a better choice, such as f_π , in future studies in three-flavor QCD.

We estimate the relevant LECs in a similar way to that for $\langle r^2 \rangle_{V,S}$ and c_V , and obtain

$$\bar{l}_6 = 11.9(0.7)(1.0), \quad (49)$$

$$\bar{l}_4 = 4.09(50)(52), \quad (50)$$

$$\bar{l}_1 - \bar{l}_2 = -2.9(0.9)(1.3), \quad (51)$$

$$r_{V,r}^r = -1.0(1.0)(2.5) \times 10^{-5}, \quad (52)$$

$$r_{V,c}^r = 4.00(17)(64) \times 10^{-5}, \quad (53)$$

$$r_{S,r}^r = 1.74(36)(78) \times 10^{-4}. \quad (54)$$

Our estimate of \bar{l}_6 is slightly smaller than those from two-loop ChPT analyses of experimental data; $\bar{l}_6 = 16.0(0.9)$ from F_V [16] and $15.2(0.4)$ from τ and π decays [57]. This is partly due to

the deviation of F between our lattice determination [5] and two-loop ChPT [51]. We note that \bar{l}_4 is consistent with our lattice determination $\bar{l}_4 = 4.12(56)$ from F_π [5] and a phenomenological estimate $4.39(22)$ [50]. Here we list $\bar{l}_1 - \bar{l}_2$ instead of $l_{1,2}^r$, which is scale invariant and equals to $(\bar{l}_1 - \bar{l}_2)/(6N)$ in the convention of Eq. (44). Although $\bar{l}_1 - \bar{l}_2$ has a large uncertainty of $\sim 50\%$, it is consistent with $-4.67(60)$ from phenomenology. Note that we set the renormalization scale $\mu = 4\pi F$, and our fit favors small values of the order of $10^{-4} - 10^{-5}$ for the renormalized $O(p^6)$ couplings $r_{\{V,S\},\{r,c\}}^r$ at this scale. Finally, we emphasize that the simultaneous fit only to $\langle r^2 \rangle_V$ and c_V without any phenomenological input leads to consistent results for the vector channel, namely for $\langle r^2 \rangle_V$, c_V , \bar{l}_6 , $\bar{l}_1 - \bar{l}_2$ and $r_{V,\{r,c\}}^r$.

VI. CONCLUSIONS

In this article, we present a lattice calculation of the pion form factors $F_{V,S}(q^2)$ in two-flavor QCD. We study the chiral behavior of the radii $\langle r^2 \rangle_{V,S}$ and the curvature c_V based on ChPT up to two loops. We employ the overlap quark action, which has exact chiral symmetry and thus provides the cleanest framework for the study of chiral behavior. Otherwise, the explicit chiral symmetry breaking of conventional lattice actions could make studies based on two-loop ChPT substantially complicated. Another salient feature of this work is that, for the first time, $F_S(q^2)$ is evaluated including the contributions of the disconnected diagrams through the all-to-all quark propagators.

Our detailed analysis based on ChPT reveals that two-loop contributions are important to describe the chiral behavior of $\langle r^2 \rangle_{V,S}$ and c_V at our simulated quark masses, which are comparable to those in recent unquenched simulations. Through the chiral extrapolation at two loops, we obtain $\langle r^2 \rangle_{V,S}$ and c_V at the physical point, which are consistent with experiment. We also obtain estimates of $O(p^4)$ and $O(p^6)$ LECs, and confirm that $F_S(q^2)$ and F_π lead to consistent results for \bar{l}_4 as suggested long ago [14].

As we already outlined in Ref. [28], the curvature c_V is useful to stabilize the two-loop chiral fit. The single pole ansatz Eq. (37), which has been commonly used in previous studies, may not be suitable to estimate c_V , since it simply assumes a relation $c_V = (\langle r^2 \rangle_V / 6)^2$ at simulated quark masses. In this work, instead, we employ a generic form up to cubic corrections to parametrize the q^2 dependence of $F_{V,S}(q^2)$ thanks to the precise determination of $F_{V,S}(q^2)$ through the all-to-all propagator. Dispersive analyses of the q^2 dependence, model independent information

of scalar resonances, and the twisted boundary condition [58] already used in Refs.[26, 27] are interesting subject and technique for a better control of this parametrization in future studies.

Extending this study to three-flavor QCD is important for more realistic comparison with experiment. We have already started simulations in three-flavor QCD with the overlap action [1, 2]; measurements of pion correlators using all-to-all propagators are in progress.

Finally, it is expected from our chiral extrapolation that $\langle r^2 \rangle_S$ shows a strong quark mass dependence due to the one-loop chiral logarithm below $M_\pi \sim 250$ MeV. Pushing simulations toward such small quark masses is an interesting subject in future studies for a direct observation of the one-loop logarithm, although it is very challenging.

Acknowledgments

Numerical simulations are performed on Hitachi SR11000 and IBM System Blue Gene Solution at High Energy Accelerator Research Organization (KEK) under a support of its Large Scale Simulation Program (No. 08-05). This work is supported in part by the Grant-in-Aid of the Ministry of Education (No. 18340075, 18740167, 19540286, 19740160, 20025010, 20039005, 20105001, 20105002, 20105003, 20105005, 20340047, 20740156 and 21684013), the National Science Council of Taiwan (No. NSC96-2112-M-002-020-MY3, NSC96-2112-M-001-017-MY3, NSC97-2119-M-002-001), and NTU-CQSE (No. 97R0066-65 and 97R0066-69).

-
- [1] H. Matsufuru, PoS **LATTICE 2007**, 018 (2007) [arXiv:0710.4225 [hep-lat]].
 - [2] S. Hashimoto, PoS **LATTICE 2008**, 011 (2008) [arXiv:0811.1257 [hep-lat]].
 - [3] R. Narayanan and H. Neuberger, Nucl. Phys. **B443**, 305 (1995) [arXiv:hep-th/9411108].
 - [4] H. Neuberger, Phys. Lett. B **417**, 141 (1998) [arXiv:hep-lat/9707022]; *ibid.* B **427**, 353 (1998) [arXiv:hep-lat/9801031].
 - [5] J. Noaki *et al.* (JLQCD and TWQCD collaborations), Phys. Rev. Lett. **101**, 202004 (2008) [arXiv:0806.0894 [hep-lat]].
 - [6] H. Fukaya *et al.* (JLQCD collaboration), Phys. Rev. Lett. **98**, 172001 (2007) [arXiv:hep-lat/0702003].
 - [7] H. Fukaya *et al.* (JLQCD and TWQCD collaborations), Phys. Rev. D **76**, 054503 (2007) [arXiv:0705.3322 [hep-lat]].
 - [8] S. Aoki *et al.* (JLQCD and TWQCD collaborations), Phys. Lett. B **665**, 294 (2008) [arXiv:0710.1130 [hep-lat]].

- [9] H. Fukaya *et al.* (JLQCD collaboration), Phys. Rev. D **77**, 074503 (2008) [arXiv:0711.4965 [hep-lat]].
- [10] S. Aoki *et al.* (JLQCD collaboration), Phys. Rev. D **77**, 094503 (2008) [arXiv:arXiv:0801.4186 [hep-lat]].
- [11] E. Shintani *et al.* (JLQCD collaboration), Phys. Rev. Lett. **101**, 242001 (2008) [arXiv:0806.4222 [hep-lat]].
- [12] H. Ohki *et al.* (JLQCD collaboration), Phys. Rev. D **78**, 054502 (2008) [arXiv:0806.4744 [hep-lat]].
- [13] E. Shintani *et al.* (JLQCD and TWQCD collaborations), arXiv:0807.0556 [hep-lat].
- [14] J. Gasser and H. Leutwyler, Ann. Phys. **158**, 142 (1984).
- [15] J. Gasser and U.-G. Meißner, Nucl. Phys. B **357**, 90 (1991).
- [16] J. Bijnens, G. Colangelo and P. Talavera, JHEP **9805**, 014 (1998) [arXiv:hep-ph/9805389].
- [17] J. Gasser and H. Leutwyler, Nucl. Phys. B **250**, 517 (1985).
- [18] J. Bijnens and P. Talavera, JHEP **0203**, 046 (2002) [arXiv:hep-ph/0203049].
- [19] Y. Nemoto (RBC collaboration), Nucl. Phys. B (Proc.Suppl.) **129**, 299 (2004), [arXiv:hep-lat/0309173].
- [20] J. van der Heide, J.H. Koch and E. Laermann, Phys. Rev. D **69**, 094511 (2004) [arXiv:hep-lat/0312023].
- [21] A.M. Abdel-Rehim and R. Lewis, Phys. Rev. D **71**, 014503 (2005), [arXiv:hep-lat/0410047].
- [22] F.D.R. Bonnet, R.G. Edwards, G.T. Fleming, R. Lewis, D.G. Richards (LHP collaboration), Phys. Rev. D **72**, 054506 (2005) [arXiv:hep-lat/0411028].
- [23] S. Hashimoto *et al.* (JLQCD collaboration), PoS **LAT2005**, 336 (2005) [arXiv:hep-lat/0510085].
- [24] D. Brömmel *et al.* (QCDSF and UKQCD collaborations), Eur. Phys. J. C **51**, 335 (2007) [arXiv:hep-lat/0608021].
- [25] S. Capitani, C. Gattringer and C.B. Lang (BGR collaboration), Phys. Rev. D **73**, 034505 (2006) [arXiv:hep-lat/0511040].
- [26] P.A. Boyle *et al.* (RBC and UKQCD collaborations), JHEP **0807**, 112 (2008) [arXiv:0804.3971 [hep-lat]].
- [27] R. Frezzotti, V. Lubicz, S. Simula (ETM collaboration), arXiv:0812.4042 [hep-lat].
- [28] T. Kaneko *et al.* (JLQCD and TWQCD collaborations), PoS **LATTICE 2008** 158, (2008) [arXiv:0810.2590 [hep-lat]].
- [29] T. Kaneko *et al.* (JLQCD collaboration), PoS **LATTICE 2007**, 148 (2007) [arXiv:0710.2390 [hep-lat]].
- [30] Y. Iwasaki, preprint UTHEP-118 (1983), unpublished.
- [31] M. Lüscher, Phys. Lett. B **428**, 342 (1998) [arXiv:hep-lat/9802011].
- [32] N. Yamada *et al.* (JLQCD collaboration), PoS **LAT2006**, 060 (2006) [arXiv:hep-lat/0609073].
- [33] S. Aoki *et al.* (JLQCD collaboration), Phys. Rev. D **78**, 014508 (2008) [arXiv:0803.3197 [hep-lat]].
- [34] Z. Fodor, S. D. Katz and K. K. Szabo, JHEP **0408**, 003 (2004) [arXiv:hep-lat/0311010].
- [35] P. M. Vranas, arXiv:hep-lat/0001006; Phys. Rev. D **74**, 034512 (2006) [arXiv:hep-lat/0606014].
- [36] H. Fukaya *et al.* (JLQCD collaboration), Phys. Rev. D **74**, 094505 (2006) [arXiv:hep-lat/0607020].

- [37] R. Brower, S. Chandrasekharan, J. W. Negele and U.-J. Wiese, Phys. Lett. B **560**, 64 (2003) [arXiv:hep-lat/0302005].
- [38] S. Aoki, H. Fukaya, S. Hashimoto and T. Onogi, Phys. Rev. D **76**, 054508 (2007) [arXiv:0707.0396 [hep-lat]].
- [39] R. Sommer, Nucl. Phys. B **411**, 839 (1994) [arXiv:hep-lat/9310022].
- [40] J. Foley *et al.* (TrinLat collaboration), Comput. Phys. Commun, **172**, 145 (2005) [arXiv:hep-lat/0505023].
- [41] N. Cundy *et al.*, Comput. Phys. Commun. **165**, 221 (2005) [arXiv:hep-lat/0405003].
- [42] L. Giusti, P. Hernandez, M. Laine, P. Weisz and H. Wittig, JHEP **0404**, 013 (2004) [arXiv:hep-lat/0402002].
- [43] T.A. DeGrand, S. Schaefer, Comput. Phys. Commun. **159**, 185 (2004) [arXiv:hep-lat/0401011].
- [44] S. Hashimoto *et al.*, Phys. Rev. D **61**, 014502 (1999) [arXiv:hep-ph/9906376].
- [45] T.B. Bunton, F.-J. Jiang and B.C. Tiburzi, Phys. Rev. D **74**, 034514 (2006) [arXiv:hep-lat/0607001, Erratum-ibid. D **74**, 099902 (2006)].
- [46] B. Borasoy and R. Lewis, Phys. Rev. D **71**, 014033 (2005) [arXiv:hep-lat/0410042].
- [47] D. Bećirević and G. Villadoro, Phys. Rev. D **69**, 054010 (2004) [arXiv:hep-lat/0311028].
- [48] C.T. Sachrajda and G. Villadoro, Phys. Lett. B **609**, 73 (2005) [arXiv:hep-lat/0411033].
- [49] C. Amsler *et al.* (Particle Data Group), Phys. Lett. B **667**, 1 (2008).
- [50] G. Colangelo, J. Gasser and H. Leutwyler, Nucl. Phys. B **603**, 125 (2001) [arXiv:hep-ph/0103088].
- [51] G. Colangelo and S. Dürr, Eur. Phys. J. C **33**, 543 (2004) [arXiv:hep-lat/0311023].
- [52] B. Ananthanarayan and S. Ramanan, arXiv:0811.0482 [hep-ph].
- [53] F.-K. Guo, C. Hanhart, F.J. Llanes-Estrada and U.-G. Meißner, arXiv:0812.3270 [hep-ph].
- [54] P. Masjuan, S. Peris and J.J. Sanz-Cillero, Phys. Rev. D **78**, 074028 (2008) [arXiv:0807.4893 [hep-ph]].
- [55] A. Bazavov *et al.* (MILC collaboration), arXiv:0903.3598 [hep-lat].
- [56] C. Aubin *et al.* (MILC collaboration), Phys. Rev. D **70**, 094505 (2004) [arXiv:hep-lat/0402030].
- [57] M. González-Alonso, A. Pich and J. Prades, Phys. Rev. D **78**, 116012 (2008) [arXiv:0810.0760 [hep-ph]].
- [58] P.F. Bedaque, Phys. Lett. B **593**, 82 (2004) [arXiv:nucl-th/0402051].